Journal of Power Sources 681 (2026) 240184

Contents lists available at ScienceDirect

Journal of Power Sources

journal homepage: www.elsevier.com/locate/jpowsour

From Microstructure to Macroscopic Performance: An optimization pipeline for solid oxide fuel cell microstructures

Eric Langner [a,*], Jakub Lengiewicz [b], Artem Semenov [a], Ahmed Makradi [b], Sylvain Gouttebroze [c], Gaston Rauchs [b], Qian Shao [d], Heinz A. Preisig [e], Thomas Wallmersperger [a], Salim Belouettar [b], Mohamed El Hachemi [b]

[a] TU Dresden, Institute of Solid Mechanics, George-Bähr-Straße 3c, Dresden, D-01069, Germany
[b] LIST, 5, Avenue des Hauts Fournaux, Esch/Alzette, L-4362, Luxembourg
[c] SINTEF, P.O. Box 4760, Torgarden, Trondheim, NO-7465, Norway
[d] Wuhan University, Department of Engineering Mechanics, School of Civil Engineering, Hubei, Wuhan, 430072, China
[e] NTNU, P.O. Box 8900, Torgarden, Trondheim, NO-7491, Norway

HIGHLIGHTS

- Flexible and multiscale optimization pipeline for solid oxide fuel cells.
- Integration of experiments, microstructure reconstruction, and multiphysics modeling.
- Application of sophisticated simulation chains to optimize the Ni-YSZ anode.
- Machine learning surrogate models for optimal electrode microstructure design.
- Validation of fast and accurate framework to maximize the power density of the cell.

GRAPHICAL ABSTRACT

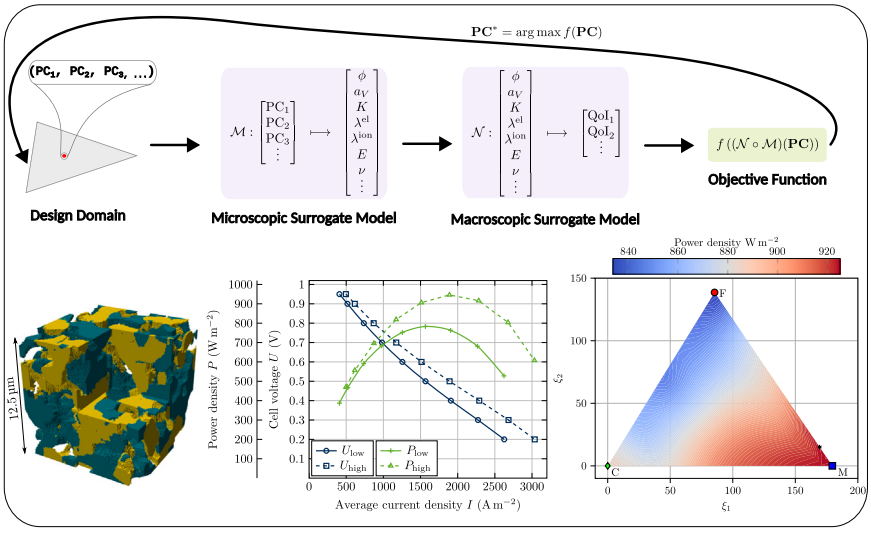

ARTICLE INFO

Keywords:
Optimization pipeline
Solid oxide fuel cells
Electrode microstructure
Multiscale modeling
Multiphysics modeling
Surrogate modeling

ABSTRACT

The rise in global carbon dioxide levels necessitates efficient, low-pollution energy technologies. Solid Oxide Fuel Cells (SOFCs) are promising energy converters, and their electrical performance is strongly influenced by the electrode microstructure. This study presents a comprehensive multiscale, experimentally grounded optimization pipeline for SOFC electrodes to maximize the electrical power density, integrating microscale and macroscale approaches. The methodology combines tomography-based microstructure characterization, computational homogenization, multiphysics simulations, model order reduction, and machine-learning-based

* Corresponding author.
E-mail addresses: eric.langner@tu-dresden.de (E. Langner), salim.belouettar@list.lu (S. Belouettar).

https://doi.org/10.1016/j.jpowsour.2026.240184
Received 3 February 2026; Received in revised form 6 April 2026; Accepted 19 April 2026
Available online 8 May 2026

surrogate modeling. Anode samples with fine, medium, and coarse grain sizes are analyzed using high-dimensional morphological descriptors to characterize microstructure morphology. Partial least squares discriminant analysis reduces the descriptor space to enable efficient surrogate modeling and generation of artificial microstructures by interpolation in the reduced space. Effective conductivities and permeability are computed by first-order homogenization and incorporated into a macroscopic fuel cell model to predict the power density. The proposed framework links microstructural information to macroscopic electrical performance within a nested optimization loop, enabling systematic exploration of physically realistic microstructural variants. Using a Ni-YSZ anode as a case study, the approach identifies the most suitable microstructure characteristics within an experimentally limited design space and provides a flexible optimization framework that can be adapted to different databases, models, and objective functions.

1. Introduction

In light of the recently published data from the World Meteorological Organization indicating the largest one-year increase in carbon dioxide in 2024 since modern measurements began, there is an urgent need for renewable and low-polluting energy generation technologies [1]. Solid oxide fuel cells (SOFCs) are promising energy converters for the future because they can generate electricity efficiently and in an environmentally friendly manner [2,3].

A SOFC module contains multiple stacks that are connected in parallel to increase the total power output. A single stack consists of several planar (or tubular) SOFC cells connected in series through metallic interconnects. In addition to the interconnects, the sandwich structure includes an anode, a dense electrolyte, and a cathode layer to facilitate electrochemical reactions. The porous nature of the electrodes ensures fluid transport towards the electrolyte. Fig. 1 summarizes the different scales of the structure of the SOFC module.

The commercialization of solid oxide fuel cells depends on improvements in performance, durability, reliability, and cost. Among the many design variables involved, the electrode microstructure plays a central role. In particular, the microstructure strongly affects the electrochemical power density of the cell. While mechanical failures, such as cracks caused by thermomechanical stresses [6] and inelastic deformations [7], as well as electrical degradation caused by redox reactions and microstructural evolution [8], are important challenges for SOFC lifetime [9], the present study focuses specifically on the optimization of the electrode microstructure with respect to electrical output performance. Therefore, mechanical stability, stress evolution, and durability are not treated as optimization objectives in this work, and must be addressed in future studies.

Multiple studies address the optimization at multiple scales, including (i) cell geometry, (ii) operating conditions, (iii) microstructural design of each individual layer, and (iv) system-level costs. Therefore, different flow field designs were compared to maximize the total collected current and improve the power density distribution [10]. In addition, a topology optimization method was used to optimize the SOFC flow channel design [11]. Artificial neural networks (ANNs) [12] and Bayesian optimization [13] were used to find the optimal operating conditions within a wide range of parameters. An enhanced configuration of the structural design of a single SOFC, such as the thickness of the electrodes and of the electrolyte, allows maximizing the electrochemical performance of the cell [14–16]. On larger scales, multi-objective optimization approaches are employed for the design of hybrid solid oxide fuel cell–gas turbine power plants, since the costs of combined heat and power are minimized while retaining high electrical efficiencies [17,18].

Besides the macroscopic improvements of the cell, the microstructures of the electrodes and their characteristics are known to have a significant impact on electrochemical performance [19,20]. For example, (i) the volume fractions of the composite constituents and of the pores [21], (ii) the length of the triple phase boundary (TPB) where electrochemical reactions occur [22], (iii) the tortuosity and percolation of each phase [23], and (iv) the particle and pore size distributions [24] all influence key microstructural characteristics. These factors determine the effective transport properties and active reaction sites that are crucial for electrical efficiency.

From an experimental point of view, Faes et al. [25] tried to optimize widely used Ni-YSZ (nickel-yttria stabilized zirconia) anodes with respect to their redox stability to counteract their low tolerance to oxidizing and reducing atmosphere changes. Connor et al. [26] developed methodologies for impregnating electrode skeletons in order to create new electrode materials and structures rapidly and cost-effectively, to find suitable solutions that improve the performance. Bischof et al. [27] aimed to determine both the optimal thickness and processing conditions for a three-layered anode with an electrochemically active Ni-GDC (nickel-gadolinia-doped ceria) area in close proximity to the electrolyte. Moreover, the manufacturing process can also be optimized by adjusting the temperature at which the powder coarsens during sintering. This affects the porosity, mechanical strength, thermal expansion, electrical conductivity, and gas permeability [28]. Recently, Lee et al. [29] investigated the effect of the pore size of anodic aluminium oxide substrates that influences the microstructural properties and thus, the electrochemical performance. This experimental approach could achieve Ni-YSZ anodes with low tortuosity and high performance at lower operating temperatures. These experimental investigations and findings contribute to the production of optimized electrode microstructures. However, due to the vast parameter space in the morphological description of the electrodes, it is not feasible to optimize the microstructure with respect to the electrochemical performance and failure probability of a single cell or stack solely through experimentation. Thus, multiscale and multiphysics approaches in combination with sophisticated simulation chains and artificial neural networks are valuable in studying the impact of various microstructural features and processing conditions to enable optimization tasks [30,31].

The optimization of electrode microstructures through theoretical calculations dates back to Kleitz and Petitbon [32], who stated that duplex SOFC electrodes, which are formed of a thin active electrode layer with a porous collecting layer, exhibit excellent performance characteristics. Jeon et al. [33] revealed the optimal combination between the mean particle diameter and the thickness of the cathode functional layer in a two-layer cathode to maximize the performance based on a micromodel. A genetic algorithm was employed to find suitable particle size distributions and porosities for both electrodes to maximize the cell performance [34]. The total resistance of the cathode was minimized due to the effects of varying porosity, thickness, particle size ratio, and volume fraction of solid particles for a given set of operating conditions, as described in [35]. In Sebdani et al. [36], more than 400 virtual realizations of a Ni-YSZ anode microstructure were generated using the Monte Carlo methodology with the objective of maximizing the TPB length at specific volume fractions. Therefore, an ANN and a genetic algorithm were applied to determine the inputs for the microstructure generation approach. To reduce the operating temperature, Abdullah and Liu [37] used a multiscale model to reveal that the power output of the cell can be maintained at lower temperatures by using nonlinear particle-size and porosity graded electrodes. Furthermore, Hasanabadi et al. [38] manipulated the two-point correlation function as a morphological descriptor to generate three-dimensional porous microstructures with diverse properties. The objective of this study was to minimize the solid-phase tortuosity and maximize the active interfacial area of

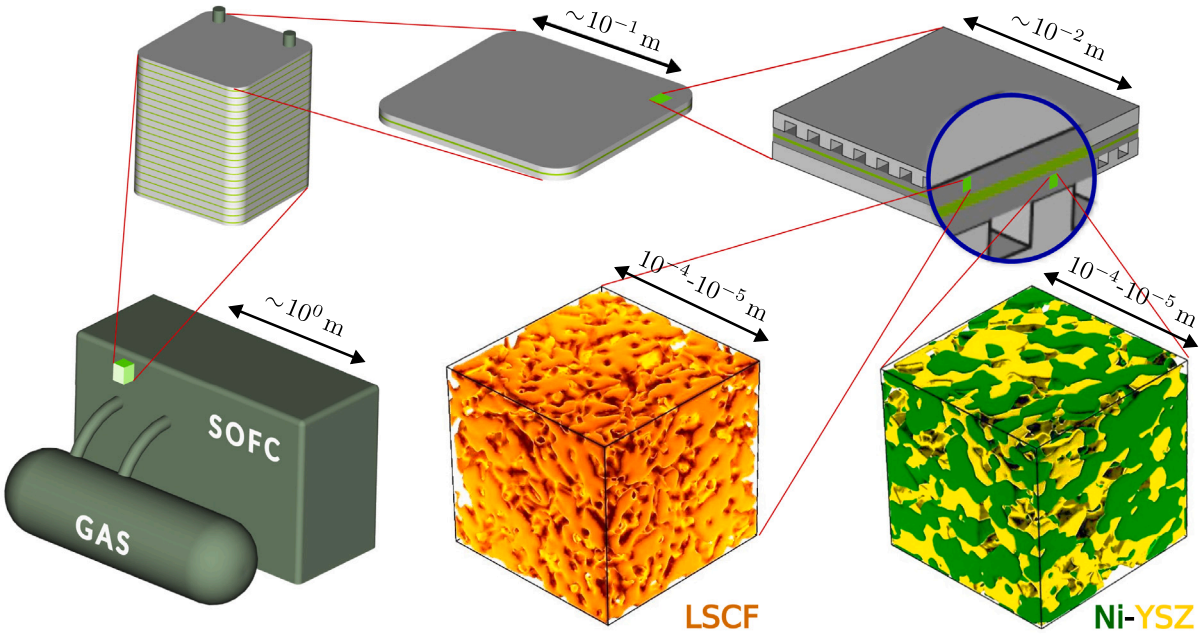

Fig. 1. Multiscale nature of Solid Oxide Fuel Cells (SOFCs). The system-level design ($\sim 10^{0}$ m) is composed of stack-level structures ($\sim 10^{-1}$ m), with single-cell internal layers present at the lower scale ($\sim 10^{-2}$ m). The characteristic scale of microstructure of the electrodes $\sim 10^{-4} - 10^{-5}$ m, with Nickel (Ni) and Yttria-Stabilized Zirconia (YSZ) phases in the anode (Ni-YSZ), and mixed-conductive lanthanum strontium cobaltite ferrite (LSCF) phase for the cathode. The red zoom-ins indicate the hierarchical connection between scales (figure motivated by [4], with Ni-YSZ reconstructed microstructure data taken from [5]). (For interpretation of the references to color in this figure legend, the reader is referred to the web version of this article.)

the void and solid phases to minimize the characteristic impedance of the cathode. Highly sophisticated simulation chains are presented in the works of Buchaniec et al. [39] and Yan et al. [40]. In [39], various microstructures were generated using the cellular automata method. 16 microstructural parameters, such as the volume fractions, the mean particle diameter and its standard deviation, the tortuosity, as well as the TPB length, were calculated for these microstructures and incorporated into a physical model to predict the performance of the anode. Additionally, evolutionary algorithms (i.e., a genetic algorithm and a particle swarm optimization) were employed to identify the optimized microstructure that maximizes the current density for a given polarization. In [40], the effect of the fabrication process with respect to powder forming, followed by sintering and operation processes, is simulated. Therefore, 770 microstructures are numerically synthesized using the discrete element and the kinetic Monte Carlo method. Electrochemical models predicted the electrode overpotential by the lattice Boltzmann method. A multilayered ANN was generated based on the simulation data to correlate the powder properties to the overpotential and the degradation rate. A multi-objective genetic algorithm was employed to minimize the two objectives. In [41], the thermal expansion properties of periodic 2D microstructures were computed using asymptotic homogenization. The microstructure was optimized to minimize the mismatch between the thermal expansion coefficients of the cathode and the electrolyte, thereby reducing mechanical stresses in the layers. Another approach in [42] was to mimic the processes from fabrication to operation for functionally graded LSCF cathodes to minimize their overpotential. A multi-objective optimization was recently solved in [43] by maximizing the power and minimizing the failure probability of the cell. Therefore, 22 microscopic parameters and varied thicknesses of the layers are implemented in a macroscopic thermo-electro-chemo-mechanical model, followed by a structural optimization using random forest and genetic algorithms as machine learning models.

Although existing approaches have demonstrated the importance of microstructural features, many rely on (i) idealized, parameterized microstructures, (ii) large, synthetic datasets, or (iii) optimization variables that are not directly tied to experimentally observed morphologies. One remaining challenge is to optimize the performance of macroscopic fuel cells within a morphological descriptor space linked to real, tomographically measured microstructures, while also enabling the systematic and realistic exploration of nearby design variants.

To address this gap, the present work introduces a novel multiscale optimization pipeline that systematically integrates experimental data, microstructural analysis, descriptor-space reduction, generative microstructure reconstruction, and performance prediction. This pipeline is designed to be flexible. In other words, the methods used in the present paper can be exchanged for other suitable simulation techniques. This pipeline starts with the high-dimensional characterization of real SOFC electrodes. The microstructures are obtained using focused ion beam–scanning electron microscopy (FIB-SEM) tomography. This technique yields three-dimensional representations of the actual electrode microstructures, capturing the precise morphology of phases at the microscale. The 3D scans establish an experimentally achievable design space, reflecting variations from different materials and fabrication processes, which form the foundation for generative microstructure reconstruction methods. From the FIB-SEM data, high-dimensional, translation-invariant morphological descriptors are extracted. These descriptors include (i) volume fractions, such as porosity and nickel content, (ii) two-point correlation and lineal-path functions, (iii) percolation factors, (iv) tortuosity, (v) double and triple phase boundaries, (vi) the particle and pore size distribution, and (vii) the shape of the particles. Since the descriptor array can contain thousands of entries, Partial Least Squares Discriminant Analysis (PLS-DA), a supervised variant of principal component analysis (PCA), is employed to reduce the descriptor space dimensionality to a few principal components (PCs) [44]. This reduction retains information about specific class labels, such as the grain size used during manufacturing. The low-dimensional principal component space, derived from experimental fine, medium, and coarse-grained Ni-YSZ microstructures [5], is then interpolated to artificially reconstruct new microstructures, effectively enlarging the dataset for training surrogate models. The microstructural properties are incorporated into a macroscopic multifield model to

compute key indicators, such as the power density of a single SOFC. This study optimizes the Ni-YSZ anode microstructure represented in the reduced descriptor space. The objective function maximizes the cell's electrical output performance. The core innovation of the proposed framework lies in its combination of experimentally measured microstructures, descriptor-based dimensionality reduction, generative reconstruction, and multiscale performance evaluation within a single, nested, two-scale optimization pipeline. This systematic approach, grounded in experimental realizations, facilitates the exploration and identification of promising microstructural configurations. Using the optimization of a Ni-YSZ anode as a case study, the proposed framework identifies the most suitable microstructural features within a limited design space to maximize the electrochemical power density under identical operating conditions. The optimized microstructure reaches a maximum power density of $P^{\max} \approx 927\,\mathrm{W\,m^{-2}}$, which is about 1 % higher than that of the morphologically closest medium-grained reference and exceeds the fine-grained and coarse-grained reference microstructures by more than 10 % and about 4 %, respectively.

The present paper is structured as follows: Section 2 details the multiscale optimization pipeline from tomography images to power output and its inverse transformation. Section 3 covers microstructure characterization and reconstruction, including dimensionality reduction to handle high-dimensional descriptors. Section 4 explains the multiscale and multiphysics modeling of SOFCs, with microscale effective property determination and macroscale power density prediction. Section 5 applies this framework to optimizing a Ni-YSZ anode. Finally, Section 6 concludes the present research.

2. Experimentally grounded optimization pipeline

The performance of SOFCs is determined by the architecture and composition of their electrodes. Various fabrication techniques, such as sintering, enable the realization of anodes and cathodes with diverse morphologies and phase distributions. Each fabrication route, through particular control over the composition and processing parameters (e.g., sintering temperature, particle size distribution, porosity control), gives rise to distinct microstructural configurations. These microstructures, in turn, determine the effective transport properties, double- and triple-phase boundary densities, and overall electrochemical performance of the cell. Understanding and controlling the interplay between the fabrication parameters, the resulting microstructure, and the functional performance remains one of the central challenges in SOFC materials optimization.

Ideally, one would establish a direct quantitative relationship between fabrication conditions and SOFC cell performance, enabling predictive optimization of the cell manufacturing process. Specifically, the sintering conditions, as well as the initial powder size and distribution, could be optimized to, for example, maximize the cell's power density. However, such a relationship is difficult to retrieve due to the complexity of coupled phenomena occurring across multiple length scales and time scales. To this end, as a first step towards this goal, the present work focuses on studying already fabricated electrodes through their high-resolution characterization. Specifically, focused ion beam–scanning electron microscopy (FIB–SEM) tomography is employed to reconstruct three-dimensional representations of the real electrode microstructures, capturing the spatial organization of constituent phases at the submicron scale.

The resulting 3D scans provide a comprehensive dataset of experimentally achievable electrode architectures, encompassing variations resulting from different material systems, fabrication parameters, and process conditions. Such a database establishes a representative library that reflects the current experimental design space of SOFC electrodes. It can serve as a foundation for a generative modeling framework aimed at exploring new/hypothetical microstructures at points interpolated between the experimentally observed ones. It allows for the synthesis of virtual microstructures with tunable properties, effectively bridging the gap between discrete experimental realizations. Such an approach allows systematic exploration of the microstructural design space that is grounded in experimental realizations, facilitating identification of promising configurations that may also be experimentally attainable.

In the following, we introduce a novel multiscale optimization pipeline that integrates the experimentally acquired data, microstructural analysis, generative modeling, and performance prediction. As a result, this will provide a closed-loop approach to SOFC electrode design and optimization.

2.1. Overview of the pipeline

The proposed optimization framework is designed as a two-scale pipeline, integrating information from both the microscale (electrode microstructure) and the macroscale (cell-level performance) to enable data-driven optimization of SOFC electrodes. The overall workflow, depicted in Fig. 2, couples experimentally derived data, computational modeling, and machine learning-based surrogate modeling (see also Section 2.2) into a unified optimization loop. The two main components – the microscale and macroscale pipelines – operate sequentially and are closely connected. This allows microstructural information to propagate to the device level and performance indicators to be fed back, enabling optimal microstructure design to be guided.

2.1.1. Microscale surrogate pipeline

At the microscale (see Fig. 2(a)), the workflow begins with the experimental FIB-SEM tomography of real SOFC electrode samples, which provides a detailed reconstruction of the microstructure. From these 3D volumes, comprehensive microstructure descriptors are derived to encode the essential morphological and spatial features quantitatively. These descriptors include both low-order characteristics (e.g., phase fractions, triple-phase boundary density) and higher-order statistical measures such as the two-point correlation function, which encodes the spatial organization of phases. The resulting descriptor vector provides an accurate but high-dimensional representation of the microstructure, and can exceed 10^4 components depending on the number of voxels of the microstructure representation.

Due to the high dimensionality of the descriptor space, model order reduction (MOR) is required prior to sampling or generative modeling. Several dimensionality reduction techniques can be applied, including Proper Orthogonal Decomposition (POD) [45], Partial Least Squares Discriminant Analysis (PLS-DA, see Section 3) [46,47], and deep neural network (DNN) autoencoders [48–52]. These techniques project (back and forth) between high-dimensional descriptor vector and their reduced latent space while pertaining to the dominant modes of microstructural variability.

Once the reduced-order representation is obtained, sampling from this reduced space – guided by probability distributions estimated from the experimental dataset – is possible. This enables the generation of new, physically plausible microstructure descriptors. Each sampled descriptor is then passed to a generative model (e.g., the one described in Section 3), which reconstructs an artificial microstructure with properties corresponding to those encoded in the descriptor. The reconstruction step for a large representative volume element is computationally expensive, often requiring several hours per sample, but it provides the necessary bridge between the descriptor space and realistic geometries.

The numerically reconstructed sampled microstructures are subsequently analyzed via computational homogenization using the finite element method, see Section 4.1. This simulation phase yields effective physical and electrochemical properties, such as porosity, electronic and ionic conductivities, and densities of the double-phase boundary (DPB) and triple-phase boundary (TPB). Together, the reduced-order descriptors and the homogenized properties form input–output pairs that populate a dataset for training a microscale surrogate model. This surrogate model – implemented, for instance, using kernel ridge regression (KRR), Gaussian process regression (GPR), or deep neural networks (see Section 2.2) – provides a fast mapping between the microstructural descriptors and the corresponding effective properties.

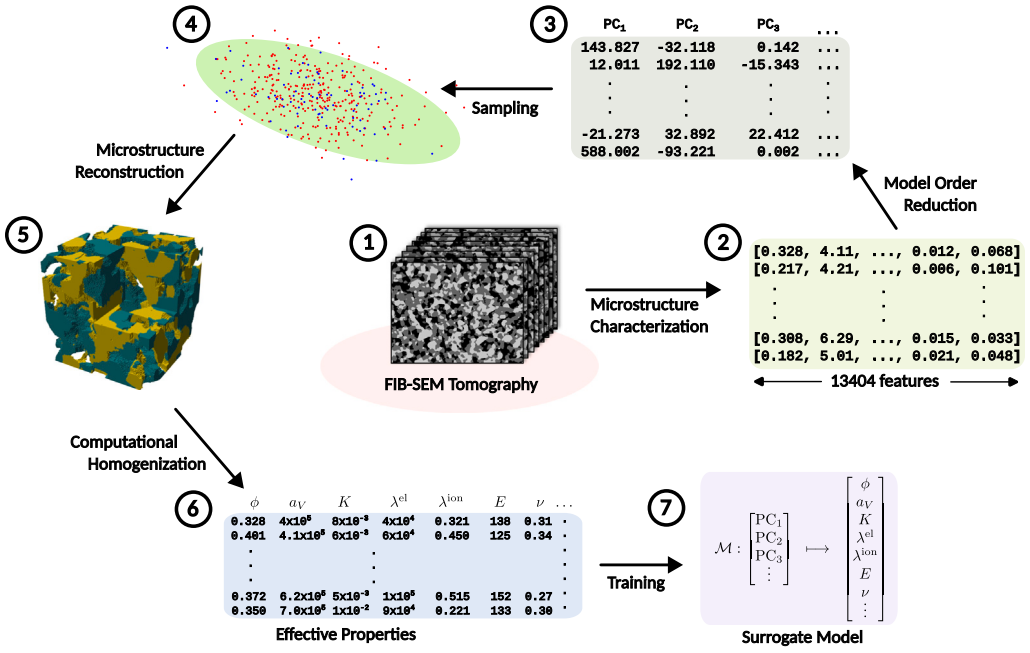

(a) Main stages of the microscale surrogate pipeline.

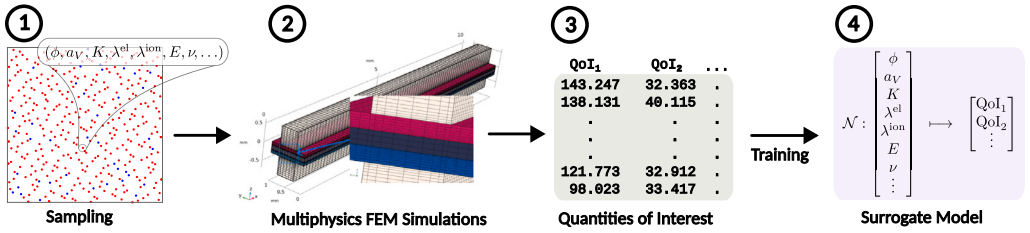

(b) Main stages of the macroscale surrogate pipeline.

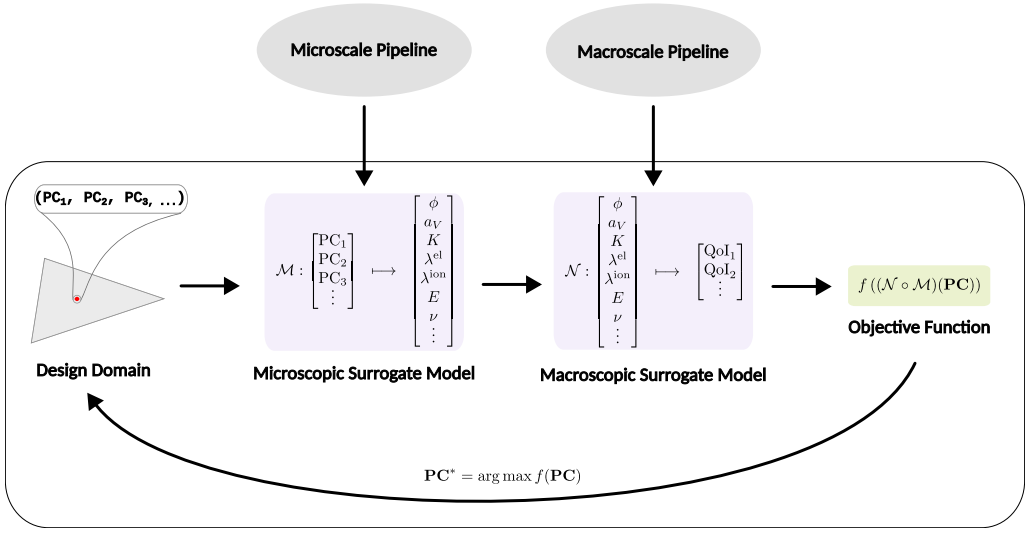

(c) Two-scale optimization loop incorporating the microscale and macroscale surrogate pipelines.

Fig. 2. Overall optimization pipeline. (For interpretation of the references to color in this figure legend, the reader is referred to the web version of this article.)

2.1.2. *Macroscale surrogate pipeline*

At the macroscale, see Fig. 2(b), a finite element model of a single SOFC cell is employed. This model incorporates the microstructural parameters obtained from the microscale pipeline (Section 2.1.1), together with other necessary inputs such as additional effective properties, material constants of the macroscopic model, geometrical parameters, and boundary conditions. The FEM analysis – outlined in more detail in Section 4.2 – provides macroscopic quantities of interest (QoI),

including current density distribution, voltage-current characteristics, maximum power density, maximum mechanical stresses, and inelastic strains of the cell.

To construct a computationally efficient macroscopic surrogate model, sampling is performed within the space of microstructural parameters derived from the microscale pipeline. The sampling range may be broad, providing a foundation for a comprehensive macroscopic surrogate model capable of coupling with different families of microstructures. The variable inputs to the macroscopic model, together with the resulting quantities of interest obtained from FEM simulations, constitute the dataset used to train the macroscopic surrogate.

Optionally, additional parameters of the macroscopic model can be included in the sampling process. Although this would allow for a more comprehensive optimization, it would also increase the dimensionality of the sampling space and, consequently, the computational cost associated with generating the surrogate model.

2.1.3. Two-scale integration and optimization loop

By coupling the microscale and macroscale surrogates, outlined in Sections 2.1.1 and 2.1.2, a nested two-scale model is established that directly links reduced-order microstructural descriptors to macroscopic performance indicators. As such, the combined surrogate serves as an efficient forward model, capable of predicting cell-level performance based solely on microstructural parameters. The surrogate serves as the main ingredient of the optimization loop (see Fig. 2(c)) to identify optimal microstructural configurations, such as those that maximize the cell's power density while possibly considering fabrication or design constraints.

In the optimization process in Fig. 2(c), the unknowns (design parameters) are the principal components, PC_i, which span the reduced-order microstructural design space. The objective function, $f(\cdot)$, is formulated in terms of quantities of interest (QoI) predicted by the nested surrogate model. This model is expressed as a composition of the microscale surrogate $\mathcal{M}$ and the macroscale surrogate $\mathcal{N}$, such that

$$f(\mathbf{QoI}(\mathbf{PC})) = f((\mathcal{N}\circ\mathcal{M})(\mathbf{PC})). \tag{1}$$

The optimization problem is thus defined as finding an approximation of the global optimizer, $\mathbf{PC}^*$, of the objective function

$$\mathbf{PC}^* = \arg\max_{\mathbf{PC}} f(\mathbf{QoI}(\mathbf{PC}))\ , \tag{2}$$

or $\arg\min$, depending on the chosen performance metric.

To compute the global optimum, various iterative procedures can be applied, including gradient-free evolutionary strategies capable of operating efficiently in reduced-order yet potentially non-convex design spaces. In this work, we employ the Differential Evolution (DE) algorithm [53], which demonstrated robust convergence behavior and is also used in the illustrative application presented in Section 5.

Because microstructure generation and homogenization are computationally intensive, a staggered optimization scheme is employed. Initially, a coarse sampling of the microscale latent space provides a sparse dataset that is adequate to locate a proxy optimum, $\mathbf{PC}^*$. The sampling is then refined adaptively in the vicinity of this preliminary optimum, and the microscopic surrogate, $\mathcal{M}'$, is retrained (or updated) to improve the predictive accuracy in that region. The refined surrogate is subsequently used to identify an improved optimum, $\mathbf{PC}^{**}$. This iterative upsampling-optimization can be repeated multiple times, potentially around several promising sub-optimal regions, enabling progressive convergence towards a globally optimal microstructural design.

2.2. Kernel-based surrogate modeling

Surrogate modeling is a powerful approach to approximate computationally expensive simulations with fast-to-evaluate models. Popular techniques include polynomial chaos expansions [54], radial basis function interpolation [55], support vector regression, and neural networks [56–60]. Among these, Gaussian Process Regression (GPR) [61] has emerged as a particularly attractive method [62–67] because it provides not only a prediction of the output but also an associated measure of uncertainty. This makes GPR especially useful in engineering design and uncertainty quantification, where both accuracy and reliability of predictions matter. In contrast to black-box approaches such as neural networks, GPR is nonparametric, relatively interpretable, and strongly rooted in Bayesian inference.

GPR can be understood as a stochastic extension of Kernel Ridge Regression (KRR): if one removes the stochastic component from the Gaussian prior over functions, the resulting estimator coincides with KRR [61]. This duality provides a useful perspective when selecting a surrogate model. While GPR offers predictive uncertainty and is therefore well suited for problems where uncertainty quantification is required, KRR provides a simpler and computationally more efficient alternative that can be advantageous in optimization settings involving repeated model evaluations. In the present work, this formulation is used as a general framework. The specific choice of surrogate model (GPR or KRR), kernel parameters, and preprocessing steps depends on the application and is detailed in Section 5.3. In particular, in the present study, the surrogate models are implemented using KRR, while GPR is retained as a general reference framework.

Formally, we are given a training dataset of size N, consisting of inputs

$$\boldsymbol{X} = \{\boldsymbol{x}_i\}_{i=1}^N, \quad \boldsymbol{x}_i \in \mathbb{R}^d, \tag{3}$$

and outputs

$$\boldsymbol{Y} = \{y_i\}_{i=1}^N, \quad y_i \in \mathbb{R}, \tag{4}$$

where each input, $\boldsymbol{x}_i$, is a vector of parameters of dimension d, while each scalar output, y_i, corresponds to a selected component of the multi-dimensional response vector. For practical reasons, for multi-output cases, we train multiple independent surrogate predictors – one per each output dimension. In both KRR and GPR, the predictor for an unknown input, $\boldsymbol{x}^*$, can be expressed in the form

$$y^*(\boldsymbol{x}^*) = \sum_i k(\boldsymbol{x}^*, \boldsymbol{x}_i)\cdot\alpha_i, \tag{5}$$

where $k(\cdot,\cdot)$ is the kernel function, see below, and $\boldsymbol{\alpha}\in\mathbb{R}^N$ is obtained by solving the linear system

$$(\boldsymbol{K} + \lambda\mathbf{I})\boldsymbol{\alpha} = \boldsymbol{Y}, \tag{6}$$

with kernel matrix $K_{ij} = k(\boldsymbol{x}_i, \boldsymbol{x}_j)$ and $\lambda \geq 0$ is the regularization parameter. In GPR, λ corresponds to the assumed noise variance, while in KRR it serves as a regularization parameter.

In practice, kernel methods are sensitive to the scaling of the input and output variables. Therefore, normalization or standardization is typically applied prior to training to ensure numerical stability and balanced contributions of all input dimensions.

A central modeling choice is the selection of the kernel function $k(\cdot,\cdot)$. The widely used squared exponential or radial basis function (RBF) kernel assumes very smooth functions, which may lead to overly optimistic extrapolations in the presence of limited or irregular data. Instead, we adopt the Matérn kernel [61,68], which introduces an additional parameter that controls the smoothness of the kernel function, allowing for a flexible control over its regularity. In particular, the 3/2 Matérn kernel (7), which is commonly used in practice due to its balance between flexibility and regularity, corresponds to once mean-square differentiable functions and takes the form:

$$k(\boldsymbol{x},\boldsymbol{x}') = k_{3/2}(r) = \sigma^2\left(1+\frac{\sqrt{3}\,r}{\ell}\right)\exp\left(-\frac{\sqrt{3}\,r}{\ell}\right), \tag{7}$$

where $r = \|\boldsymbol{x}-\boldsymbol{x}'\|$ is the distance between the two vectors, σ^2 is the variance, and ℓ is the characteristic length scale.

In summary, surrogate models based on KRR/GPR provide a principled, kernel-based framework for approximating expensive simulations. By expressing the prediction as a linear system involving kernel evaluations, they are computationally efficient and capable of capturing nonlinearities. The choice between the GPR and KRR depends on whether uncertainty quantification is needed.

In our two-scale pipeline (Section 2.1), we employ two surrogate models. The first, the *micro-surrogate*, captures the mapping

$$\mathcal{M} : \mathcal{X}_{\text{micro}} \longrightarrow \mathcal{P}_{\text{eff}}, \tag{8}$$

where $\mathcal{X}_{\text{micro}}$ denotes the reduced-order descriptors of the anode's microstructure and $\mathcal{P}_{\text{eff}}$ the corresponding effective physical properties. These properties are then passed as inputs to the second model, the *macro-surrogate*, which is trained on a dataset generated from macroscopic SOFC simulations. Formally, it establishes the mapping

$$\mathcal{N} : \mathcal{P}_{\text{eff}} \longrightarrow \mathcal{Q}_{\text{SOFC}}, \tag{9}$$

where $\mathcal{Q}_{\text{SOFC}}$ denotes the quantities of interest that determine cell performance (e.g., the maximum average power).

3. Generative microstructure reconstruction of 3D anode microstructures

Reconstructing realistic three-dimensional (3D) microstructures of SOFC anodes is a critical yet computationally demanding task within the multiscale optimization pipeline. These reconstructions are required to generate statistically representative microstructural domains that mirror the morphological features observed in experimental imaging, such as those obtained via focused ion beam-scanning electron microscopy (FIB-SEM) or X-ray nano-tomography.

This section briefly summarizes the procedure to numerically generate microstructures of SOFC electrodes. The reconstructions represent RVEs, which serve as an input for predicting the effective properties. In addition, the dimensionality reduction of the morphological descriptors is explained.

To reconstruct realistic microstructures, experimental FIB-SEM data are analyzed from a statistical perspective. Therefore, the voxel-based microstructure $\boldsymbol{M}$ is morphologically characterized by translation-invariant descriptors $\boldsymbol{D}$. Thus, the characterization function $\boldsymbol{f_C}$ maps $\boldsymbol{M}$ to a set of n_D stationary descriptors by

$$\boldsymbol{f_C} \; : \; \boldsymbol{M} \mapsto \{\boldsymbol{D}_i\}_{i=1}^{n_D} \; . \tag{10}$$

The statistical descriptors include (i) the volume fractions of each phase p, (ii) the two-point functions, i.e., the two-point correlation function and the lineal-path function, to describe the shape and size of the grains, (iii) the percolation of each phase to the necessary components of the fuel cell, (iv) the tortuosity of each phase p and each direction, and (v) the double and triple phase boundaries, respectively. These high-dimensional descriptors determine the effective physical properties of the electrode.

The microstructure reconstruction process is a two-step optimization procedure: It starts with the differentiable microstructure characterization and reconstruction (DMCR) approach, followed by the Yeong–Torquato algorithm. DMCR efficiently generates morphologically plausible solutions, while the second step reduces noise and fine-tunes certain descriptors, and thus improves the solution. Both methods rely on the optimization problem

$$\boldsymbol{M}^{\text{rec}} = \arg\min_{\boldsymbol{M}} \mathcal{L}\left(\{\boldsymbol{D}_i(\boldsymbol{M}), \boldsymbol{D}_i^{\text{des}}\}_{i=1}^{n_D}\right) \tag{11}$$

to generate a numerically reconstructed microstructure $\boldsymbol{M}^{\text{rec}}$ with desired descriptors $\boldsymbol{D}_i^{\text{des}}$. The loss function that needs to be minimized can be calculated by the weighted sum of mean squared errors (MSE) between the real descriptor after each iteration $\boldsymbol{D}_i$ and the desired $\boldsymbol{D}_i^{\text{des}}$:

$$\mathcal{L}(\boldsymbol{M}) = \sum_{i=1}^{n_D} \|\boldsymbol{D}_i - \boldsymbol{D}_i^{\text{des}}\|_{\text{MSE}} \; . \tag{12}$$

Details on the descriptors, characterization, reconstruction process, and the limits of this reconstruction method for SOFC electrodes can be found in our previous work [69]. The computational expense associated with generative microstructure reconstruction is substantial. Generating a single high-resolution three-dimensional sample typically requires approximately 24 h of dedicated computation on a single NVIDIA A100 (40 GB HBM2) GPU. The computational cost of the reconstruction process scales with both the domain size and the desired statistical fidelity.

Since the length of the descriptor array contains several thousand entries (depending on the number of voxels of the microstructure and the type and number of descriptors), the dimensionality of $\boldsymbol{D}$ needs to be reduced. Partial least squares discriminant analysis (PLS-DA) [46,47] – a supervised version of principal component analysis – computes new features in the reduced space, known as principal components (PCs) [44]. The method reduces the dimensionality while retaining information about certain class labels, such as the grain size used in the manufacturing process. Thus, the PLS-DA retains as much of the covariance between the original data and its labeling as possible in the first PCs. The PCs can be calculated as the eigenvalues of the covariance matrix $\boldsymbol{C}$ calculated by

$$\boldsymbol{C} = \frac{1}{(n-1)^2} \boldsymbol{X}^T \boldsymbol{C}_n \boldsymbol{y} \boldsymbol{y}^T \boldsymbol{C}_n \boldsymbol{X} \; . \tag{13}$$

Here, $\boldsymbol{X} \in \mathbb{R}^{n \times m}$ is a matrix with n samples and m-dimensional descriptor entries, $\boldsymbol{C}_n \in \mathbb{R}^{n \times n}$ is the centering matrix to remove the mean of the data, and $\boldsymbol{y}$ is the labeling vector that contains information about the particular class (e.g., Coarse, Medium, Fine). The number of principal components that must be considered depends on the variance included in each PC. The results of the reduction in dimensionality for anode microstructures manufactured with different grain sizes can be found in Section 5.1.

4. Multiscale and multiphysics modeling of solid oxide fuel cells

This section outlines the methodology used to determine the effective properties are determined (Section 4.1) and of the macroscopic model (Section 4.2) used to compute the fuel cell performance, taking into account geometry, operating conditions, and effective physical parameters.

4.1. Effective properties

To accurately capture the influence of the microstructure on the SOFC behavior, the effective transport properties must be determined. Therefore, first-order computational homogenization is applied similarly to our previous works [69,70]. The physical transport properties of the electrode – thermal conductivity, electrical conductivity, ionic conductivity, and fluid permeability – are computed using FEniCSx [71], a Python-based open-source finite element tool. The 3D microstructure samples that are artificially generated serve as representative volume elements (RVEs) and are discretized into hexahedral finite element meshes. The selected RVEs are assumed to be sufficiently large to ensure statistical representativeness. If the microstructure exhibits strong heterogeneities over the total domain of the electrode, as specifically shown for cathodes in Mahbub et al. [72], multiple RVEs need to be defined. The locally varying effective properties can be implemented in macroscopic models to better capture such heterogeneous structures. Specific material properties are assigned to each phase of the microstructure, such as thermal and electrical conductivity. Periodic boundary conditions are applied for all microscale problems as part of a first-order homogenization to satisfy the Hill–Mandel conditions, ensuring the energy equivalence between the microscale and macroscale. For the microscopic analysis, effective second-order tensors are obtained to account for general anisotropy. As the material behavior is linear, three independent macroscopic loading cases are required for computing

the macroscopic material response. Thus, the solutions can be used to represent the effective macroscopic material behavior.

For the thermal conductivity, the heat conduction equation

$$-\nabla \cdot (\boldsymbol{\kappa}(T) \cdot \nabla T) = 0 \tag{14}$$

with Fourier's law is solved, where T is the temperature and $\boldsymbol{\kappa}$ the thermal conductivity tensor. More specifically, the temperature T is split into the operating temperature T_{op}, a macroscopic temperature gradient $\overline{\nabla T}$ and a fluctuating part $\widetilde{T}$: $T = T_{\mathrm{op}} + \overline{\nabla T} \cdot \boldsymbol{x} + \widetilde{T}$. The fluctuation is solved while enforcing periodicity. Similarly, the effective electrical conductivity can be extracted by solving the continuity equation with Ohm's law

$$-\nabla \cdot (\lambda^{\mathrm{el}}(T) \cdot \nabla \phi_{\mathrm{s}}) = 0\,, \tag{15}$$

where λ^{el} is the electric conductivity tensor. The macroscopic ionic conductivity is calculated after solving the charge balance of charged ions

$$-\nabla \cdot \left(\lambda^{\mathrm{ion}}(T) \cdot \nabla \phi_{\ell}\right) = 0 \tag{16}$$

with λ^{ion} being the conductivity of oxygen ions. Furthermore, ϕ_{s} and ϕ_{ℓ} are the electric potential in solid conductors and the electric potential in the electrolyte phase. In the Eqs. (15) and (16), the potentials are additively decomposed into macroscopic gradients $\overline{\nabla \phi}_{\ell/\mathrm{s}}$ and fluctuations $\widetilde{\phi}_{\ell/\mathrm{s}}$. The homogenized values of the potential gradients and the flow of electrons and ions are used to evaluate the effective conductivities.

The Stokes equations for an incompressible fluid flow are solved on the microscale to approximate the fluid permeability on the macroscale:

$$\nabla \cdot \boldsymbol{v} = 0\,, \quad \nabla \cdot (-p\boldsymbol{I} + 2\mu(T)\,\boldsymbol{d}) = \boldsymbol{0}\,. \tag{17}$$

Here, $\boldsymbol{v}$ is the fluid velocity, p the fluid pressure, μ the dynamic viscosity, $\boldsymbol{I}$ the unity tensor, and $\boldsymbol{d}$ the strain rate tensor. The pressure can be expressed by $p = \overline{\nabla p} \cdot \boldsymbol{x} + \widetilde{p}$. The periodicity is fulfilled for both the velocity and the pressure. The homogenized solutions of the pressure $\langle p \rangle$ and the velocity $\langle \boldsymbol{v} \rangle$ are used to calculate the effective permeability tensor $\boldsymbol{K}^{\mathrm{eff}}$ using Darcy's law with $\langle \boldsymbol{v} \rangle = \frac{\boldsymbol{K}^{\mathrm{eff}}}{\mu} \langle \nabla p \rangle$. Iterative solvers are employed to efficiently compute the respective physical quantities under imposed gradients on high-resolution meshes. The validity of the morphological features (e.g., the specific surface area) and effective physical properties is confirmed by comparing our results to empirical equations [22] and reporting values from the literature [73,74].

4.2. Macroscopic modeling

In this section, the coupled electrochemical-fluid flow model used to compute the current densities for specific operating conditions and polarizations is adapted from previous studies [7,30]. The equations and couplings between the physical fields are summarized as follows:

The charge balances (Eqs. (18) and (19)) describe the transport of ions and electrons through the layers of the fuel cell:

$$\frac{\partial \rho^{\mathrm{el}}}{\partial t} - \nabla \cdot \left(\lambda^{\mathrm{el,eff}} \cdot \nabla \phi_{\mathrm{s}}\right) = \dot{Q}^{\mathrm{el}}\,, \tag{18}$$

$$\frac{\partial \rho^{\mathrm{ion}}}{\partial t} - \nabla \cdot \left(\lambda^{\mathrm{ion,eff}} \cdot \nabla \phi_{\ell}\right) = \dot{Q}^{\mathrm{ion}}\,. \tag{19}$$

Here, $\rho^{\mathrm{el}}, \rho^{\mathrm{ion}}$ denote the electronic and ionic charge densities, $\lambda^{\mathrm{el,eff}}$, $\lambda^{\mathrm{ion,eff}}$ are the effective electronic and ionic conductivity tensors, and $\dot{Q}^{\mathrm{el}}, \dot{Q}^{\mathrm{ion}}$ the charge carrier sources, which are the coupling terms due to electrochemical reactions as:

$$\underbrace{\dot{Q}^{\mathrm{el}} = -i\,,\ \dot{Q}^{\mathrm{ion}} = i}_{\text{at the anode}}\,, \quad \underbrace{\dot{Q}^{\mathrm{el}} = i\,,\ \dot{Q}^{\mathrm{ion}} = -i}_{\text{at the cathode}}\,, \quad \underbrace{\dot{Q}^{\mathrm{el}} = \dot{Q}^{\mathrm{ion}} = 0}_{\text{elsewhere}}\,. \tag{20}$$

There are various modeling approaches to describe the kinetics of electrochemical reactions, which can be categorized into the activation-controlled and the diffusion-controlled Butler–Volmer equations, see Eqs. (21) and (22), respectively [73].

$$i = a_{\mathrm{V}} \cdot i_0 \left(\exp\left(\frac{\beta_{\mathrm{a}} F \eta}{RT}\right) - \exp\left(\frac{-\beta_{\mathrm{c}} F \eta}{RT}\right)\right) \tag{21}$$

$$i = a_{\mathrm{V}} \cdot i_{0,\mathrm{ref}} \left(\frac{x_{\mathrm{O,TPB}}}{x_{\mathrm{O,b}}} \exp\left(\frac{\alpha_{\mathrm{a}} F \eta_{\mathrm{ref}}}{RT}\right) - \frac{x_{\mathrm{R,TPB}}}{x_{\mathrm{R,b}}} \exp\left(\frac{-\alpha_{\mathrm{c}} F \eta_{\mathrm{ref}}}{RT}\right)\right) \tag{22}$$

In these equations, a_{V} is the specific surface area, F the Faraday constant, R the universal gas constant, T the temperature, $\alpha_{\mathrm{a}}, \beta_{\mathrm{a}}$ and $\alpha_{\mathrm{c}}, \beta_{\mathrm{c}}$ the anodic and cathodic charge transfer coefficients, $\eta, \eta_{\mathrm{ref}}$ the overpotential, and $x_{\mathrm{O}}, x_{\mathrm{R}}$ the mole fractions of the oxidized and the reduced species at the triple phase boundary (TPB) and in the bulk gas phase, respectively. The exchange current density $i_0, i_{0,\mathrm{ref}}$ is often determined empirically and is different for different fuel cell designs. Typically, these parameters are calibrated with experimental results. For the generation of data, the activation-controlled reaction kinetics (21) is used, where the exchange current density is related to the concentration of redox species using the partial pressures with:

$$i_{0,\mathrm{e}} = i_{0,\mathrm{ref}} \prod_{i:\nu_i>0} \left(\frac{p_i}{p_{i,\mathrm{ref}}}\right)^{\frac{a_{\mathrm{c}}\nu_i}{n_{\mathrm{e}}}} \prod_{i:\nu_i<0} \left(\frac{p_i}{p_{i,\mathrm{ref}}}\right)^{\frac{-a_{\mathrm{a}}\nu_i}{n_{\mathrm{e}}}}\,. \tag{23}$$

By inserting the stoichiometry ν_i of the species, we end up with the kinetics for the anode and cathode, respectively, using n_{e} as the number of electrons transferred per mole of reaction:

$$i_{0,\mathrm{c}} = i_{0,\mathrm{ref}} \left(\frac{p_{\mathrm{O_2}}}{p_{\mathrm{O_2,ref}}}\right)^{\frac{a_{\mathrm{c}}}{n_{\mathrm{e}}}}\,, \tag{24}$$

$$i_{0,\mathrm{a}} = i_{0,\mathrm{ref}} \left(\frac{p_{\mathrm{H_2}}}{p_{\mathrm{H_2,ref}}}\right)^{\frac{a_{\mathrm{c}}}{n_{\mathrm{e}}}} \left(\frac{p_{\mathrm{H_2O}}}{p_{\mathrm{H_2O,ref}}}\right)^{\frac{a_{\mathrm{a}}}{n_{\mathrm{e}}}}\,. \tag{25}$$

The reference exchange current density $i_{0,\mathrm{ref}}$ is based on an empirical equation by

$$i_{0,\mathrm{ref}} = \gamma \exp\left(-\frac{E_{\mathrm{act}}}{RT}\right) \tag{26}$$

with the activation energy E_{act} and a pre-exponential factor γ. Both parameters are typically fitted to experimental results, for example, in Yonekura et al. [75] and Perna et al. [76]. Please note that γ and E_{act} have wide ranges for both electrodes as they depend on both the microstructure morphology and the operating conditions, such as the temperature and the humidity of the fuel [73].

The mass balance (27) accounts for the conservation of mass for each species

$$\frac{\partial(\rho\varphi)}{\partial t} + \nabla \cdot (\rho \boldsymbol{v}) = \dot{W}, \tag{27}$$

with the porosity φ, the density ρ, the velocity $\boldsymbol{v}$ of the fluid, and the mass source term $\dot{W}$ in Eq. (28), which is responsible for the coupling to the electrochemical reactions:

$$\underbrace{\dot{W} = (M_{\mathrm{H_2O}} - M_{\mathrm{H_2}})i/(2F)}_{\text{at the anode}}\,, \quad \underbrace{\dot{W} = -M_{\mathrm{O_2}} i/(4F)}_{\text{at the anode}}\,, \quad \underbrace{\dot{W} = 0}_{\text{elsewhere}}\,. \tag{28}$$

The molecular weight of the species i is denoted by M_i. The conversion between reacting species is also considered in the linear momentum balance for the fluid, which is defined using the widely applied Brinkman equation (29):

$$\begin{aligned}\frac{\rho}{\varphi}\left[\frac{\partial \boldsymbol{v}}{\partial t} + \frac{\boldsymbol{v}}{\varphi} \cdot (\nabla \boldsymbol{v})\right] = &-\nabla p + \nabla \cdot \left[\frac{\mu}{\varphi}\left\{\nabla \boldsymbol{v} + \boldsymbol{v}\nabla - \frac{2}{3}(\nabla \cdot \boldsymbol{v})\boldsymbol{I}\right\}\right] \\ &- \left(\mu \boldsymbol{K}^{-1,\mathrm{eff}} + \frac{\dot{W}}{\varphi^2}\boldsymbol{I}\right) \cdot \boldsymbol{v} + \boldsymbol{f}\,.\end{aligned} \tag{29}$$

Here, $\boldsymbol{K}$ is the effective permeability of the porous structure, $\boldsymbol{I}$ is the unity tensor, and $\boldsymbol{f}$ is the mechanical volume force density. The species conservation (30) describes the transport of gas through the electrodes towards the electrolyte for each species i. Since the pores are small

compared to the mean free path of the gas, Knudsen diffusion combined with Fick's law is employed for the multicomponent mass transport:

$$\frac{\partial(\rho\varphi\omega_i)}{\partial t} + \nabla\cdot\left(\rho\omega_i \boldsymbol{v}\right) = \nabla\cdot\left(\rho\frac{\omega_i}{x_i}\boldsymbol{D}_i\cdot\nabla x_i\right) + \dot{R}_i \,. \tag{30}$$

Here, ω_i is the mass fraction, x_i the molar fraction, $\boldsymbol{D}_i$ the effective diffusivity tensor and $\dot{R}_i$ the mass production rate in Eq. (31) with

$$\underbrace{\dot{R}_{\mathrm{H_2}} = -M_{\mathrm{H_2}} i/(2F)\,,\ \dot{R}_{\mathrm{H_2O}} = M_{\mathrm{H_2O}} i/(2F)}_{\text{at the anode}}\,,$$
$$\underbrace{\dot{R}_{\mathrm{O_2}} = -M_{\mathrm{O_2}} i/(4F)}_{\text{at the cathode}}\,,\quad \underbrace{\dot{R}_i = 0}_{\text{elsewhere}}\,. \tag{31}$$

The balance equation to compute the temperature T is the energy balance (32) with

$$\frac{\partial(\rho C_p^{\mathrm{eff}} T)}{\partial t} + \nabla\cdot\left(\rho C_p^{\mathrm{f}} T\boldsymbol{v}\right) = \nabla\cdot(\boldsymbol{\kappa}\cdot\nabla T) + \dot{H}\,. \tag{32}$$

Here, C_p is the effective heat capacity, $\boldsymbol{\kappa}$ the effective thermal conductivity tensor, and $\dot{H}$ (Eq. (33)) the heat source that is defined by Joule heating, thermodynamic heat released by ideal reactions, and heat released for the activation of the electrochemical reaction:

$$\underbrace{\dot{H} = 0}_{\text{at gas channels}}\,,\ \underbrace{\dot{H} = \nabla\phi_\ell\cdot\lambda^{\mathrm{ion}}\cdot\nabla\phi_\ell}_{\text{at electrolyte}}\,,$$
$$\underbrace{\dot{H} = \nabla\phi_{\mathrm{s}}\cdot\lambda^{\mathrm{el}}\cdot\nabla\phi_{\mathrm{s}} + \nabla\phi_\ell\cdot\lambda^{\mathrm{ion}}\cdot\nabla\phi_\ell + \frac{i}{n_{\mathrm{e}}F}T\Delta S + i\eta}_{\text{at electrodes}}\,. \tag{33}$$

The macroscopic model is validated against experimental data [77] using material and geometric properties provided in Shao et al. [78].

5. Application to the optimization of Ni-YSZ anode microstructure

In this section, the SOFC optimization pipeline is applied to the anode as a specific layer of the fuel cell. Rather than varying the design of the fuel cell or its operating conditions, the focus is on identifying the most suitable anode microstructure to maximize the electrochemical performance of the SOFC in terms of maximum power density.

5.1. Experimentally based micro-scale data generation

The starting point for optimizing the electrode microstructure is experimental tomography data [5]. The images taken by the FIB-SEM procedure are used to reconstruct the porous anode consisting of nickel and YSZ, see Fig. 3. Composite anodes with (i) fine grain sizes, (ii) medium grain sizes, and (iii) coarse grain sizes were produced. Each anode was exposed to eight redox cycles, which is why the electrodes are already in a degraded state compared to those directly after sintering.

As discussed in Section 3, the morphological characterization of the electrodes using certain descriptors results in a large data set. It is not feasible to train the surrogate model with a very high number of input data since this would require a large amount of training data. Thus, the descriptor array is reduced to three principal components using Partial Least Squares Discriminant Analysis (PLS-DA) [46,47], as shown in Fig. 4(a). Three principal components (PCs) were chosen to be efficient, as they already contain most of the covariance between $\boldsymbol{X}$ and $\boldsymbol{y}$. More specifically, 98.5 % of the variance of the high-dimensional descriptors $\boldsymbol{X}$ and 92.9 % of the variance of the class labeling vector $\boldsymbol{y}$ is captured by three PCs. Additionally, microstructures econstructed from (i) the original descriptor and (ii) the descriptor after projection into the low-dimensional space and back-transformation exhibit very similar effective properties, within the variability of the reconstruction process itself.

In Fig. 4(a), two 2D plots can be seen with (left) the PC_1–PC_2 plane and (right) the PC_1–PC_3 plane to clearly visualize the coordinates in the reduced principal component space. From the fine microstructure, nine sections of the entire tomography data are cut to characterize each sample separately in order to have a larger number n of samples for the dimensionality reduction. Similarly, four sections of the medium and coarse microstructures are used in each case, respectively. The samples from the "Fine" class are closer together than those from the other two classes. This is due to the variability within each microstructure section: the fine-grained sample with an edge length of 9.4 µm is more statistically representative than the medium-grained microstructure with an edge length of 11.5 µm and the coarse-grained microstructure with 12.4 µm, respectively. The variability in principal component PC_3 of the coarse microstructure is particularly large, partly because PC_3 includes the least variance of the three PCs. The larger symbols with the black boundaries show the averaged points for each class, i.e., all PCs of the samples of a certain class are averaged. It is worth noting that the medium-grain-sized microstructure does not fall between the fine- and coarse-grain classes, but rather that the three averaged points (F, M, C) form a triangle in the 3D space. These points highlight the experimental truth for sampling, which will be discussed in Section 5.4.

Due to the cost and limited availability of experimental samples, microstructures are numerically reconstructed to match the statistical descriptors of the real samples, see also Section 3. In general, from a sufficiently large dataset of real microstructures, one can estimate a probability function in the reduced-dimensional space. Sampling from this distribution enables the generation of new and plausible data points that are statistically similar to the experimental observations. In the present case, since only three real microstructure samples are available, additional samples are artificially reconstructed by linear interpolation in the low-dimensional space, as it is done, e.g., in [79]. The goal is to develop morphologies that combine features of the three initial structures. The interpolation method used in the low-dimensional descriptor space serves as an approximation for generating new microstructures. However, this approach has limitations in accurately capturing the complex relationships within the high-dimensional descriptor space. In the future, it will be necessary to develop nonlinear interpolation methods that can better satisfy the descriptor relationships, such as the correlation between the two-point correlation function and the volume fraction. These advanced methods would ensure a more accurate representation of the microstructural properties and their interactions, ultimately improving the predictive capability of the generated morphologies. Two generated microstructures with fine grains and coarse grains are shown as examples in Fig. 4(b).

Although the interpolated microstructures may not fully reflect manufacturable configurations, they provide a reasonable basis for methodological development and can be refined in future work as more data are available. As improvements for the future, several points can be addressed: (i) replacing artificial microstructures with real samples as more experimental imaging data become available, (ii) developing nonlinear interpolation schemes in the reduced space, and (iii) estimating an explicit probability distribution to generate statistically plausible microstructure realizations.

5.2. Macro-scale data generation

The fuel cell model used for the macroscopic data generation is shown in Fig. 5(a). It is worth noting that the layer thicknesses of the fuel cell highly influence the electrochemical performance. Therefore, realistic anode-supported, electrolyte-supported, or cathode-supported fuel cell configurations can be employed in future studies to predict the cell power density accurately. In order to model the physical processes occurring within the fuel cell during operation, it is essential to define boundary conditions. The cell voltage difference is prescribed by defining the electric potential ϕ_{s} (i) grounded at the bottom of the anode, and (ii) as $V_{\mathrm{cell}} = 0.2\,\mathrm{V}, \ldots, 0.95\,\mathrm{V}$ along the rib side of the cathode. There is no conduction of electrons through the electrolyte membrane because dense YSZ is an insulating material. Furthermore, there are no flow conditions for ions or electrons at the outer boundaries or between

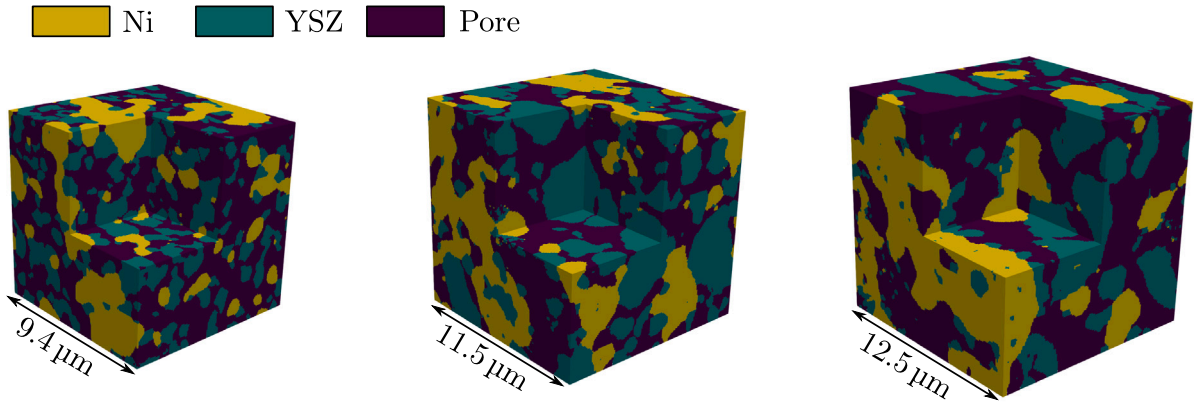

Fig. 3. Numerically reconstructed microstructures from 3D FIB-SEM tomography images by Holzer et al. [5]. The anode consists of a nickel phase, a YSZ phase, and pores. The microstructure samples were produced with (left) fine grains, (middle) medium grains, and (right) coarse grains, and were tomographed after the exposure to eight redox cycles. (For interpretation of the references to color in this figure legend, the reader is referred to the web version of this article.)

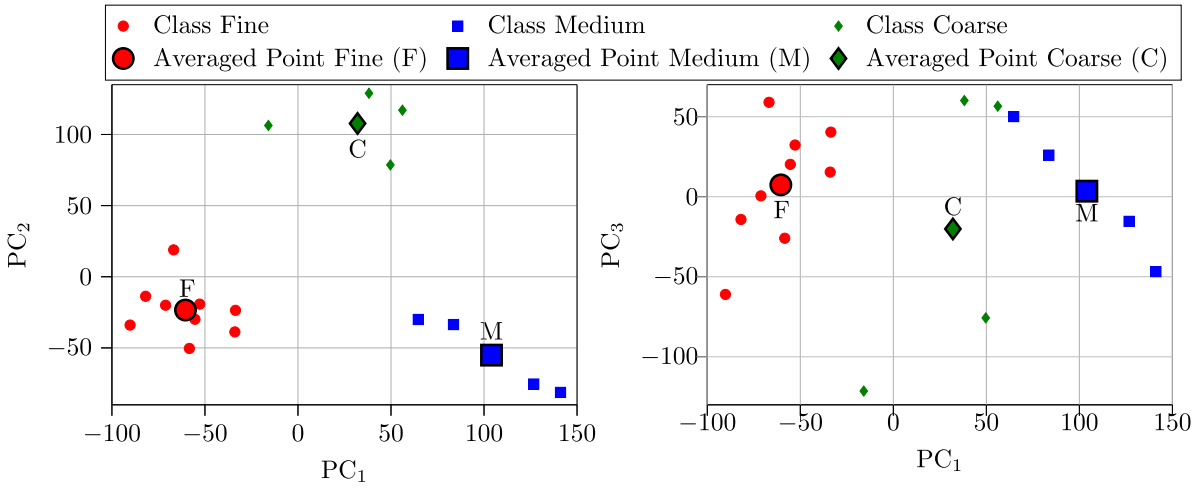

(a) Dimensionality reduction using PLS-DA for the fine-, medium-, and coarse-grained microstructures in the principal component PC_1–PC_2 plane (left) and the PC_1–PC_3 plane (right). The averaged points of each class (F, M, C) are the averaged principal components of the samples of each classified microstructure.

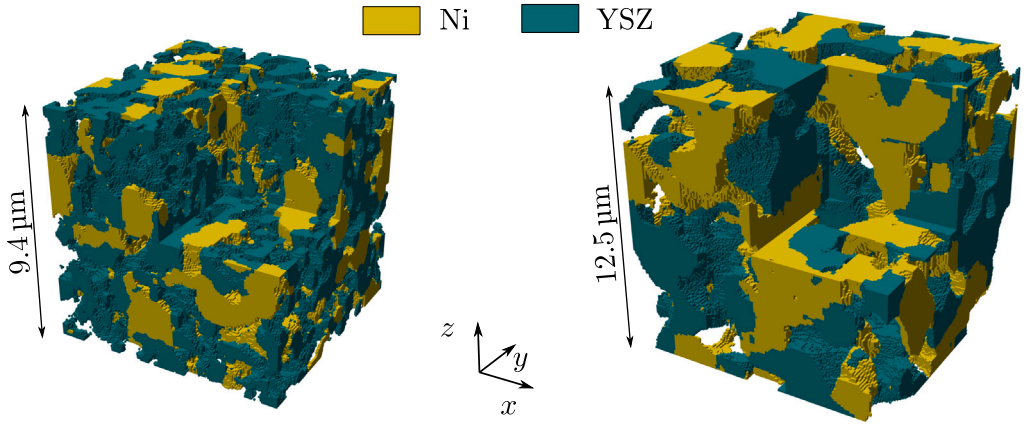

(b) Artificially generated microstructures with fine grains (left) and coarse grains (right). The anode consists of a nickel phase (yellow), a YSZ phase (green), and pores (voids).

Fig. 4. Dimensionality reduction and generative microstructure reconstructions with fine and coarse grains from principal component space. (For interpretation of the references to color in this figure legend, the reader is referred to the web version of this article.)

the electrodes and gas channels. The pressure differences between the gas channel inlets and outlets were prescribed by Dirichlet boundary conditions of 2 Pa at the anode and 6 Pa at the cathode. Slip conditions are prescribed for the fluid to the right and left of the porous electrodes, and no-slip conditions are set at the top, bottom, front, and back surfaces of the cathode and anode, as well as at the boundaries of the

gas channels. The temperature of the upstream flow of the gas channels is set to $T = 800\,°C$ at the inlets. Additionally, no heat flow in the normal direction is assumed at any of the other boundaries.

The following mass fractions of the gases are considered: $\omega_{H_2} = 0.4$ and $\omega_{H_2O} = 0.6$ at the anode side correspond to a humidified hydrogen fuel stream as well as $\omega_{O_2} = 0.227$, $\omega_{H_2O} = 0.037$ and $\omega_{N_2} = 0.736$ at the cathode side describe air intake with about 90 % relative humidity. These values are kept in all simulations to have comparable operating conditions. This enables a clear assessment of how changes in the electrode microstructure affect the cell's electrochemical power density, without interference from variations in fuel composition. These values serve as a consistent baseline for studying microstructural optimization. It should be noted that the optimal microstructure depends on operating conditions such as fuel composition and inlet flow rates. In this work, the chosen conditions are used to analyze anodes that have undergone degradation after eight redox cycles, which has a direct impact on the resulting power density.

Fig. 5(b) depicts a mid-length transverse cross-section of an electrochemical unit cell, and several key transport phenomena are visualized. The contours of the electrolyte potential ϕ_ℓ show a gradient from $-0.11\,V$ to $-0.507\,V$, due to electrochemical activity across the domain. Streamlines of current density i_ℓ reveal transversal variations in charge transfer, which influence species production and consumption. Notably, a vortex is evident in the H_2 flow field. This recirculation is likely driven by water vapor production, which causes flow interaction with density gradients between light H_2 gas and heavier H_2O vapor.

Fig. 5(c) reveals high-temperature electrochemical transport phenomena. The distribution of the electric potential ϕ_s, visualized through color contours, drives a non-uniform electronic current density i_s, which peaks sharply at the corner channel and rib–contact interface. The maximum magnitude is $i_s = 12.2\,kA\,m^{-2}$. This localization identifies regions of intensified electrochemical activity, where hydrogen oxidation (anode) and oxygen reduction (cathode) are most pronounced. At the current operating temperature, water exists exclusively as vapor, introducing strong thermal and compositional buoyancy effects. The cathode-side H_2O streamline vortex, with a flux maximum of $53.6\,g\,m^{-2}\,s^{-1}$, is therefore a result of thermal convection – where locally heated gas from exothermic reactions rises – combined with species-driven buoyancy: the lighter remaining O_2-depleted gas mixes with heavier product water vapor, creating density gradients that induce buoyancy-driven recirculation. Meanwhile, the anode side shows normal H_2O diffusion (with a maximum flux of $10\,g\,m^{-2}\,s^{-1}$), consistent with steam being a reaction product from hydrogen oxidation, carried away in the fuel stream. The observed vortex highlights the interplay between electrochemically-driven heat release, non-uniform current distribution, and high-temperature gas dynamics in SOFCs, where such recirculation can enhance local mixing and reactant access.

The morphological and physical parameters that are employed in the macroscopic physical model described in Section 4.2 are listed in Table 1. It should be noted that the anisotropies in the physical transport properties are disregarded, and isotropic estimates are employed. In addition to the anode and the cathode, the electrolyte is characterized by an ionic conductivity of $\lambda^{ion} = 1.21\,S\,m^{-1}$ and a thermal conductivity of $\kappa = 5\,W\,m^{-1}\,K^{-1}$ at $T = 800\,°C$.

As the focus is on the optimization of the anode, the properties of the cathode were kept constant, and their values are assumed from reported values [73,83]. The properties of the anode are transferred mainly from the microscopic analysis (see Section 4.1) of the samples. The active specific surface area a_V is the interface density between the nickel and YSZ particles [84,85]. This is measured for the artificially constructed microstructures. Typical values of a_V – which is in the range of $1 \cdot 10^5$ to $1 \cdot 10^7\,m^{-1}$ – can be found in [73,86]. For already degraded electrodes (after a few redox cycles), the range of the active specific area is $0.4 \cdot 10^6 - 0.7 \cdot 10^6\,m^{-1}$. This is rather low, but realistic due to the microstructural changes that are correlated with a reduction in triple phase boundary density and nickel particle coarsening. The permeability range for the anode is determined by upscaling the Stokes equations and is in very good agreement with results reported in [74,87]. The tortuosity of the porous phase $\tau^{(p)}$ for the anode is only included in the diffusion of the gaseous species, as the other effective transport properties listed in the table do not need to be modified by some empirical parameter.

The Halton sequence is employed to produce distributed points in the design space of anode parameters in order to train the macroscopic surrogate model $\mathcal{N}$. A total of 350 simulation cases were conducted to generate 270 training and 80 test data. The combination of the sampling strategy and the number of training points leads to a reliable and accurate macroscopic surrogate model, with the relative error of an average of 0.5 % in the test data.

The efficiency of the solid oxide fuel cell is demonstrated by considering the polarization (U–I) and the power density (P–I) curves. Fig. 6 exhibits the high-low performing cases in the training data. The high-performing case shows the best power output of $950 W/m^2$ and the low-performing case shows the best power output of $783 W/m^2$. The data used to generate the maximal and minimal performances is based on specific combinations of the anode microstructural parameters, see Table 1. However, the random combination of effective properties for the implementation in the macroscopic model is not physically plausible because it cannot be realized by physically admissible anode microstructures (see Section 5.4).

5.3. Surrogate model configuration and preprocessing

In the present application, both microscopic and macroscopic surrogate models are implemented using Kernel Ridge Regression (KRR) with a 3/2 Matérn kernel, see Eq. (7). While Gaussian Process Regression (GPR) provides predictive uncertainty, KRR is adopted here due to its lower computational cost and sufficient accuracy for repeated evaluations within the optimization loop, see the discussion in Section 2.2.

All input and output variables are normalized componentwise using statistics of the training data. This preprocessing improves numerical conditioning and ensures balanced scaling across the input dimensions. The same normalization is consistently applied during training and inference.

The microscopic surrogate is constructed in two stages corresponding to the coarse and refined datasets. For the coarse model, a kernel length scale of $\ell = 1.2$ is used, while for the refined (upsampled) model a smaller length scale $\ell = 0.6$ is employed to better resolve the increased density of samples in the region of interest. In both cases, the regularization parameter is set to $\lambda = 10^{-2}$. The relatively larger regularization reflects variability in the effective properties originating from the stochastic microstructure reconstruction process.

For the macroscopic surrogate, the hyperparameters are $\ell = 1.0$ and $\lambda = 10^{-5}$, corresponding to a smoother response and a lower effective noise level, since the macroscopic simulations are deterministic once the effective properties are fixed.

5.4. Microstructural optimization

The corner points of each class (Fine, Medium, Coarse) form a triangle in which 15 points are evenly distributed, see Fig. 7(a). The effective properties of these reconstructions were employed to train the microscopic surrogate model $\mathcal{M}$ for the first guess of the optimization point using a sparse data set. Additionally, 7 points for testing the surrogate model were randomly placed into the ξ_1–ξ_2 plane, which is used to project the triangular surface from the 3D to the 2D space, see Fig. 7(a). Please note that the projection onto the triangular plane of coordinates (ξ_1, ξ_2) is only for visualization purposes. The coupled surrogate framework, combined with the solution of the optimization function (see Section 2.1.3)

$$\mathbf{PC}^* = \arg\max_{\mathbf{PC}} f(\boldsymbol{P}^{\max}(\mathbf{PC})) \tag{34}$$

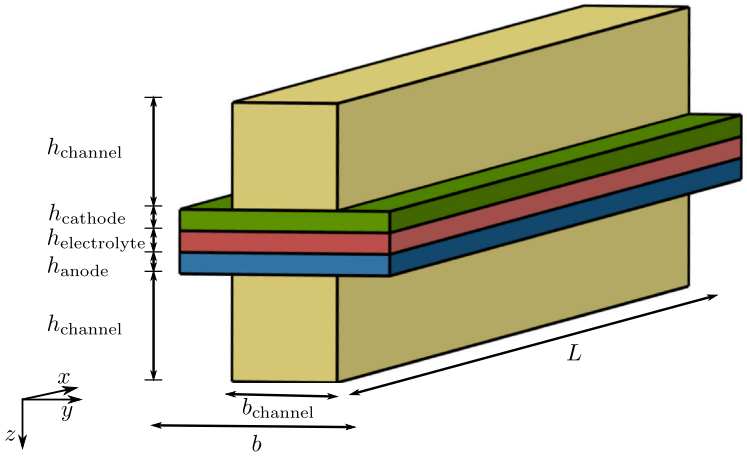

(a) Fuel cell unit model for the finite element simulation with the following dimensions: $h_{\text{channel}} = 500\ \mu\text{m}$, $h_{\text{anode}} = 100\ \mu\text{m}$, $h_{\text{cathode}} = 100\ \mu\text{m}$, $h_{\text{electrolyte}} = 100\ \mu\text{m}$, $b_{\text{channel}} = 500\ \mu\text{m}$, $b = 1\,\text{mm}$, $L = 10\,\text{mm}$.

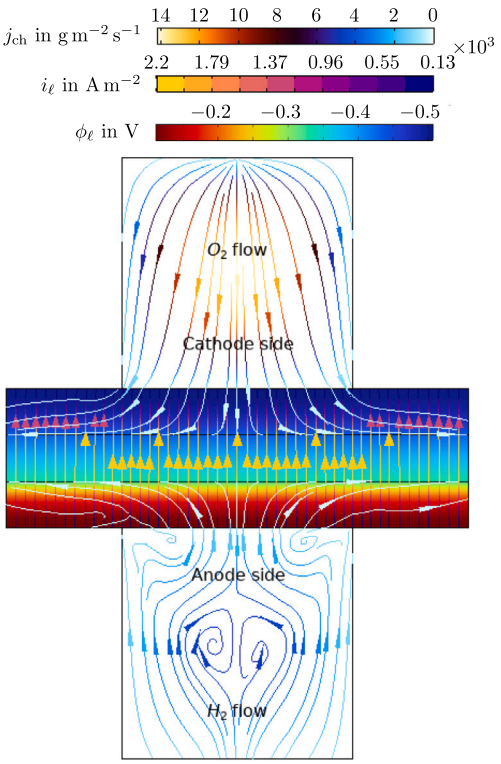

(b) The color contours show the distribution of the electrolyte potential ϕ_ℓ. The vector streamlines across the electrode depict the electrolyte current density i_ℓ. The current density is directed from the anode towards the cathode with a maximum intensity of $i_\ell = 2.2\,\text{kA m}^{-2}$ inside the membrane. The total mass flow streamlines show that the O_2 diffusion on the cathode side is uniform with a maximum of $j_{\text{ch}} = 14.1\,\text{g m}^{-2}\,\text{s}^{-1}$, while at the anode side, the H_2 streamlines show a vortex in the center with a maximum of $j_{\text{ch}} = 5\,\text{g m}^{-2}\,\text{s}^{-1}$.

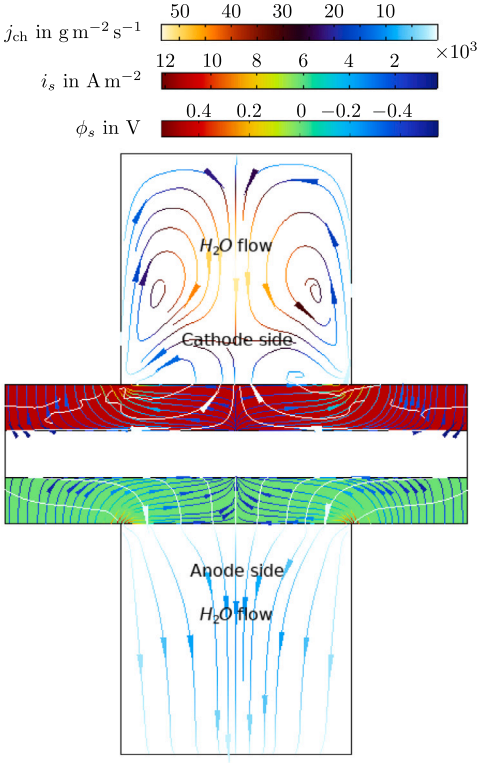

(c) The color contours show the distribution of the electric potential ϕ_s. The vector streamlines across the electrode depict the electronic current density i_s. The vector lines are directed from the center towards the polarization contacts with a maximum intensity of $i_s = 12.2\,\text{kA m}^{-2}$ at the corner channel and rib–contacts. The total mass flow streamlines show that H_2O diffusion in the anode side is normal with a flux maximum of $j_{\text{ch}} = 10\,\text{g m}^{-2}\,\text{s}^{-1}$ while at the cathode side the streamlines show a vortex in the center with a maximum of $j_{\text{ch}} = 53.6\,\text{g m}^{-2}\,\text{s}^{-1}$.

Fig. 5. Solid oxide fuel cell dimensions (a) and the cell's physical fields for a cross-section at $x = 5\,\text{mm}$ (b,c). The physical fields are evaluated for a fuel cell polarization of $V_{\text{cell}} = 0.45\,\text{V}$. (For interpretation of the references to color in this figure legend, the reader is referred to the web version of this article.)

leads to a preliminary optimal point in the three-dimensional **PC** space with a maximum power density $P^{\max} = 924.1\,\text{W m}^{-2}$ (see Fig. 7(b) for the location on the triangular domain). It is clear that the optimum point is near the experimentally derived medium average point (M). As the surrogate model for the first optimization step was trained using only a coarse data set, a circular range in the same 3D plane around

Table 1
Parameters of the cathode and the anode used in the fuel cell model to generate data for the surrogate model at a temperature of $T = 800\,°C$. The values of the cathode are taken from the literature [73,80–82]. * The values for the anode are determined by the analysis of the microstructure.

Parameter	Symbol	Unit	Cathode	Anode*
Porosity	φ^{pore}	–	0.4	0.38 – 0.5
Tortuosity of pores	τ^{pore}	–	4.0	4.0
Specific Surface Area	a_{V}	m^{-1}	$1.0 \cdot 10^{6}$	$(4 - 7) \cdot 10^{5}$
Permeability	K	μm^2	$8.0 \cdot 10^{-3}$	$(2 - 15) \cdot 10^{-3}$
Electrical conductivity	λ^{el}	S m^{-1}	$4.0 \cdot 10^{4}$	$(1 - 30) \cdot 10^{4}$
Ionic conductivity	λ^{ion}	S m^{-1}	1.0	0.2 – 0.6
Thermal conductivity	κ	$\text{W m}^{-1}\,\text{K}^{-1}$	8.0	1.5
Exchange current density	i_0	A m^{-2}	2.21	44.16
Reaction transfer	α_{a}	–	3.5	0.5
coefficients	α_{c}	–	0.5	1.5

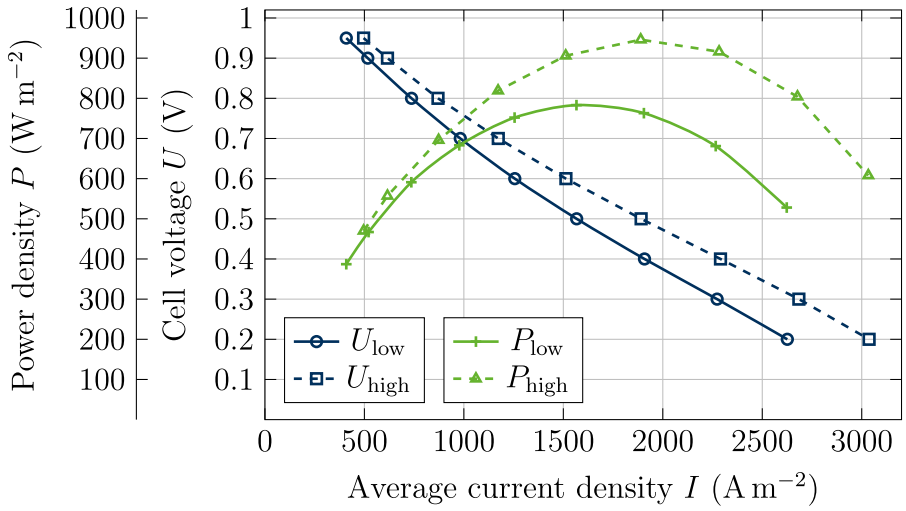

Fig. 6. Maximal and minimal SOFC performance curves: Polarization curve (U–I) and power density curve (P–I), for electrodes with properties in Table 1.

the point $\mathcal{X}^{\text{opt}}|_{\text{step=1}}$ is selected to generate additional data points. In particular, 27 data points for training and 5 data points for testing were numerically reconstructed using the method explained in Section 3, and the effective conductivities and permeabilities were computed by the homogenization method (see Section 4.1). Based on this dataset of the new sampling points, the microscopic surrogate $\mathcal{M}'$ is retrained to establish a more accurate link between the principal component space and the effective properties. Using the nested surrogate model $\mathcal{N} \circ \mathcal{M}'$ and the optimization function (34), an updated optimized point $\mathcal{X}^{\text{opt}}|_{\text{step=2}}(\mathbf{PC})$ is found, see Fig. 7(b). The first optimization step constrains the search for the optimum to the triangular domain. The second optimization step constrains the search to the circular domain around the optimum point $\chi^{\text{opt}}|_{\text{step=1}}$. Although the search space in step 2 is not restricted to the triangular domain, $\mathcal{X}^{\text{opt}}|_{\text{step=2}}$ lies in close proximity to $\mathcal{X}^{\text{opt}}|_{\text{step=1}}$ in the principal component space. The maximum power density in the power density curve is predicted to be $P^{\max}(\mathcal{X}^{\text{opt}}|_{\text{step=2}}) = 927.2\,\text{W m}^{-2}$. The color contours within the circle indicate that slight variations in the principal components of the microstructure result in noticeable changes in power density. This behavior may be further affected by the variability of the generative microstructure reconstruction method. Notably, the maximum power density corresponding to the best-performing case in Fig. 6 is not attained. This discrepancy arises because the effective properties are constrained by physically realizable microstructures. Consequently, the results indicate that arbitrary combinations of $\mathcal{P}_{\text{eff}}$ cannot be selected, as they are not realizable by the microstructure.

To assess the accuracy of the data with the proposed optimization pipeline, 20 reconstructions of the optimized point $\mathcal{X}^{\text{opt}}|_{\text{step=2}}$ are generated. Due to the variability of the reconstruction method (see Section 3 and Ref. [69] for details), every generation ends up with a different, but statistically similar microstructure. However, since the reconstruction process is also an optimization problem that is solved by a local optimization algorithm, it generally only finds local optimums instead of the global optimum. The response of the homogenization varies, resulting in a range of effective properties. Assuming an approximately normal distribution of the effective properties, the mean value μ and its standard deviation σ of each property are evaluated, which is implemented in the physical macroscopic model. The optimized anode consists of nickel with a volume fraction of $\varphi^{\text{Ni}} = (37.64 \pm 0)\%$, YSZ with $\varphi^{\text{YSZ}} = (22.24 \pm 0)\%$ and a porous volume fraction of $\varphi^{\text{pore}} = (40.12 \pm 0)\%$. The specific surface area, i.e., the interface area between Ni and YSZ, is $a_{\text{V}} = (0.567 \pm 0.008) \cdot 10^{6}\,\text{m}^{-1}$. In addition, the effective physical properties are the electronic conductivity $\lambda^{\text{el}} = (1.36 \pm 0.07) \cdot 10^{5}\,\text{S m}^{-1}$, the ionic conductivity $\lambda^{\text{ion}} = (0.384 \pm 0.009)\,\text{S m}^{-1}$, and the permeability $K = (4.115 \pm 0.171) \cdot 10^{-3}\,(\mu\text{m})^2$. The effective properties of certain reconstructions can be found in Table 3. Please note that these microstructure properties are not claimed to be the global optimum, including all possible microstructure varieties that can be fabricated. The optimal microstructure characteristics depend on the operating conditions [34]. Shi and Xue [34] found that the optimal porosities are approximately between 0.4 and 0.5, depending on the fuel composition and the inlet flow rates of the fuel and air. Additionally, Vivet et al. [21] experimentally investigated five microstructures and determined that the ideal volume fractions are $\varphi^{\text{pore}} = 41\,\%$, $\varphi^{\text{YSZ}} = 33\,\%$, $\varphi^{\text{Ni}} = 26\,\%$ to maximize triple phase boundary density and electric conductivity. In the current work, the optimization of the microstructure properties is restricted to a triangular domain. This domain can be enlarged by including more experimental FIB-SEM tomography data or numerically generated representative volume elements.

The maximum power that is achievable for a microstructure for the averaged effective properties is $P^{\max} = 925.8\,\text{W m}^{-2}$. Thus, the relative

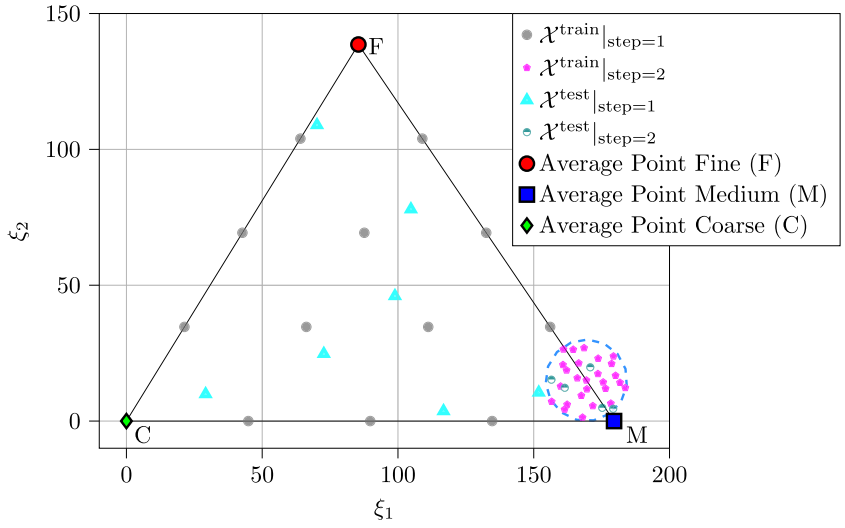

(a) Sampling points for (i) training the surrogate model between the principal components and the effective properties $\mathcal{X}^{\text{train}}$, including the averaged points of each class label, and (ii) testing the surrogate model $\mathcal{X}^{\text{test}}$ for the optimization steps 1 (triangle) and 2 (blue, dashed circle).

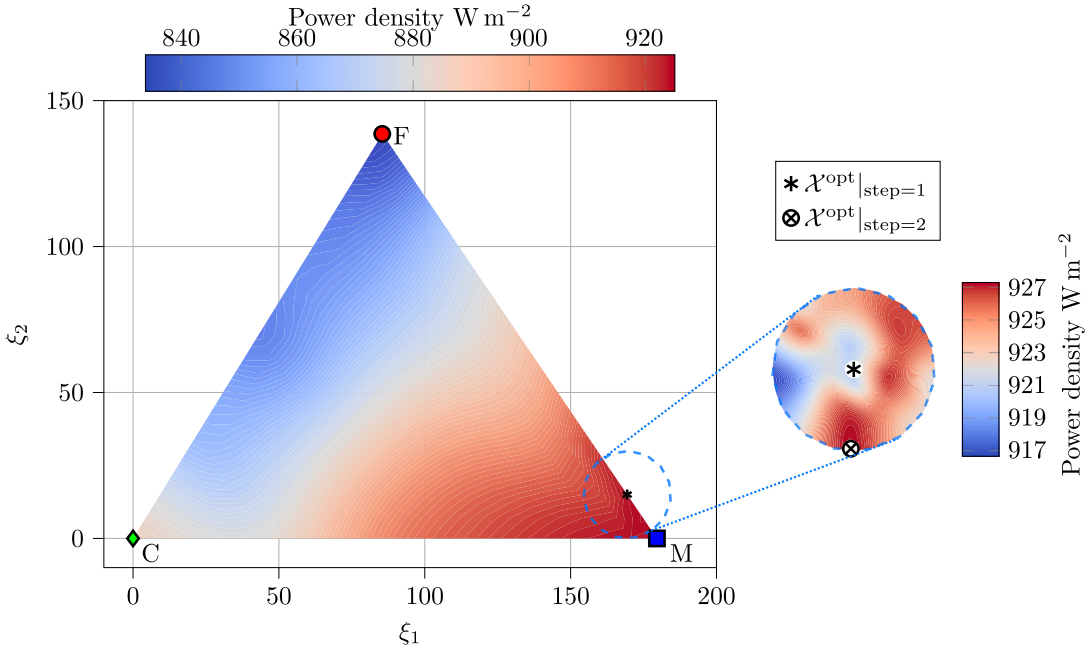

(b) Heat map of the maximum power density $P^{\max}$ predicted by (i) the coarse-data surrogate pipeline $(\mathcal{N}\circ\mathcal{M})(\mathbf{PC})$ for the triangular domain at optimization step 1, and (ii) the refined surrogate pipeline $(\mathcal{N}\circ\mathcal{M}')(\mathbf{PC})$ for the circular domain at optimization step 2. Here, $\mathcal{M}$ and $\mathcal{M}'$ represent the microscopic surrogate models trained by a coarse and a refined data set, respectively. The marked points indicate the preliminary optimum based on the coarse data and the optimized point based on the refined sampling strategy, respectively.

Fig. 7. Sampling points for the microscopic surrogate model (a), and heat map of the maximum power density (b). For visualization, the triangular domain in the 3D principal component (PC) space **PC** is projected onto the ξ_1–ξ_2 plane. (For interpretation of the references to color in this figure legend, the reader is referred to the web version of this article.)

error between the nested surrogate model and the maximum power of the reconstructions is 0.18 %. Computing the maximum power density for each of the 20 reconstructions, a mean power and its standard deviation can be calculated as $P^{\max} = (925.2 \pm 1.7)\,\mathrm{W\,m^{-2}}$. That means that the predicted $P^{\max}$ from the nested surrogates is not in the range of $\mu \pm 1.0\sigma$, but rather $\mu \pm 1.165\sigma$. Table 2 summarizes the deviations and relative errors of the microscopic surrogate model, as well as the resulting predicted maximum power density. The final error in $P^{\max}$ occurs mainly due to the deviations of the effective properties, as the macroscopic surrogate model $\mathcal{N}$ is very accurate.

To explain the trend observed in the maximum power density in Fig. 7(b), the microstructural properties of the triangular domain are analyzed. The coarse microstructure (C) exhibits the highest permeability and electrical conductivity. While the fine microstructure (F) has a higher electrical conductivity compared to the medium microstructure (M), its permeability is approximately one-third lower. The medium microstructure (M) achieves the highest power density due to its superior ionic conductivity and favorable active specific surface area. Specifically, the ionic conductivity of (M) is 25 % larger than that of (C) and 70 % higher than that of (F). Additionally, the specific surface

Table 2
Effective properties $\mathcal{P}_{\text{eff}}$ of the anode at the optimized point $\mathcal{X}^{\text{opt}}|_{\text{step}=2}$ indicated by the mean values and the standard deviations of the reconstructions $\boldsymbol{M}^{\text{rec}}$, and the predictions of the microscopic surrogate model $\mathcal{M}'$. The maximum power was calculated for the effective properties of $\boldsymbol{M}^{\text{rec}}$ and $\mathcal{M}'$ by the macroscopic surrogate model $\mathcal{N}$. The relative error is denoted by ε. The larger deviation in permeability is attributed to its high sensitivity to microstructural connectivity and reconstruction variability.

	φ^{pore} in %	a_{V} in m^{-1}	λ^{el} in S m^{-1}	λ^{ion} in S m^{-1}	K in μm^2
$\mathcal{P}_{\text{eff}}(\boldsymbol{M}^{\text{rec}})$	40.12 ± 0	$(0.567 \pm 0.008) \cdot 10^6$	$(1.36 \pm 0.07) \cdot 10^5$	(0.384 ± 0.009)	$(4.115 \pm 0.171) \cdot 10^{-3}$
$\mathcal{M}'$	40.14	$0.569 \cdot 10^6$	$1.37 \cdot 10^5$	0.391	$4.479 \cdot 10^{-3}$
ε	0.06 %	0.47 %	0.07 %	1.83 %	8.84 %

	$P^{\max}$ in W m^{-2}
$\mathcal{N} \circ \mathcal{P}_{\text{eff}}(\boldsymbol{M}^{\text{rec}})$	(925.2 ± 1.7)
$\mathcal{N} \circ \mathcal{M}'$	927.2
ε	0.18 %

area a_{V} of (M) is 134 % of that of (C) but only 85 % of (F). It is important to note that the specific surface area, often referred to as the interface area between nickel and YSZ, correlates directly with the active triple phase boundary (TPB) density. The evaluation of ρ_{TPB} reveals that (M) has twice the TPB density of (C) but only 60 % of that of (F). These findings align with the established principles that (i) ionic conductivity is an important limiting factor of electrochemical reactions, and (ii) higher TPB densities increase the number of reaction sites, enabling more simultaneous redox reactions. When comparing the medium microstructure (M) to the optimized microstructure ($\chi^{\text{opt}}|_{\text{step}=2}$), it is observed that both λ^{ion} and a_{V} remain nearly constant. However, the permeability K increases, which explains the slight improvement in power density following the optimization process.

The limited accuracy of the surrogate model arises from the variability of the effective properties of the reconstructed microstructures, combined with the relatively small number of sampling points in the circular domain. In particular, the permeability exhibits significant variability, as the tortuosity is not explicitly enforced during the reconstruction process [69]. Due to computational resources and the time requirements to generate a microstructure, only a single reconstruction is performed per sampling point. To improve the accuracy of the surrogate model $\mathcal{M}'$, a larger microscopic data set is required. This means that either multiple reconstruction processes must be carried out for each sampling point to account for variability in surrogate modeling (see Section 2.2), or the sampling distribution must be refined (i.e., increased in density). In the future, this can be obtained by experimental samples or numerically through more generated representative volume elements with faster reconstruction methods.

Overall, the results remain highly satisfactory, demonstrating the effectiveness of the optimization pipeline, and the anode microstructure can be tailored to optimize the maximum power density based on data derived from experiments. Specifically, the maximum power density is increased by approximately 1 %, 4 %, and more than 10 % relative to the medium-, coarse-, and fine-grained reference microstructures, respectively. This method can be adapted to similar two-scale optimization problems or more complex optimization functions.

5.5. Validation of the optimal microstructure solution

Twenty reconstructions of the optimized point $\mathcal{X}^{\text{opt}}|_{\text{step}=2}$ are generated based on the two-scale optimization loop illustrated in Fig. 2(c). Even though we used the same morphological descriptor to generate the optimal microstructure, the generative microstructure reconstruction methodology is not deterministic, but depends on random seeds (i.e., the initialization of the microstructure) due to the application of local optimizers. This leads to slight variations in the effective properties, see Table 3. However, the effective parameters exhibit low variability across all realizations, including porosity, specific surface area, electronic conductivity, ionic conductivity, and permeability. This confirms the robustness of the optimization pipeline and the statistical consistency of the reconstruction process.

The effective properties $\mathcal{P}_{\text{eff}}$ of the reconstructions were used as inputs for high-fidelity COMSOL Multiphysics simulations to validate the predicted performance. Comparing the results between the macroscopic physical model and the macro-surrogate model for a certain set of microstructural parameters reveals that the surrogate model can predict the maximum electrochemical power density with high accuracy. The impact and sensitivity of microstructural variations are assessed by comparing the resulting polarization (U–I) and power density (P–I) curves, shown in Fig. 8. The curves confirm that the optimized microstructures consistently achieve high power outputs with minimal performance scatter between Case 3, with maximum power of $P^{\max} = 926.85\,\text{W m}^{-2}$, and Case 14 with maximum power of $P^{\max} = 921.52\,\text{W m}^{-2}$. This validates the surrogate-based optimization. However, it should be noted that Case 14 shows the largest deviation from the average maximum power of $P^{\max,\text{avg}} = 925.2\,\text{W m}^{-2}$. As can be seen in Fig. 8, the deviation between the curves increases with increased polarization and thus, a lower cell voltage. This means that the activation polarization is highly consistent across the realizations of the optimal point. However, the Ohmic polarization is slightly different, which can be attributed to differences in transport resistances of ions and electrons. As can be seen in Table 3, the ionic conductivity of Case 14 is one of the lowest of all realizations. In addition, the permeability is also lower compared to the other reconstructions. This results in increased concentration polarizations. The combination of these two parameters results in the lowest maximum power density of the twenty reconstructions.

6. Conclusion

The present work establishes a novel multiscale optimization framework integrating microstructure reconstruction, homogenization, and surrogate-based optimization pipeline to obtain the most suitable anode microstructure for a maximum power density of the solid oxide fuel cell (SOFC) at specific operating conditions. This study is based on experimentally measured three-dimensional anodes made of nickel (Ni) and yttria-stabilized zirconia (YSZ). The microstructures are morphologically described by high-dimensional descriptors, and the effective physical properties are obtained by computational homogenization. The transport characteristics are incorporated into a multiphysics model at the single fuel cell level to compute the polarization and power density curve. To expand the database of structure–property and property–performance relationships, artificial microstructures are numerically reconstructed by interpolation within a low-dimensional principal component space. The data is employed to train microscopic and macroscopic surrogate models that are able to efficiently and accurately optimize the anode microstructure for maximum efficiency in two optimization steps. The optimal Ni-YSZ

Table 3
Parameters of the optimal anode's microstructure determined from the optimization loop.

$\mathcal{P}_{\text{eff}}$	φ^{pore} in %	a_{V} in m^{-1}	λ^{el} in S m^{-1}	λ^{ion} in S m^{-1}	K in μm^2
Case 1	40.12	$0.561 \cdot 10^6$	$1.320 \cdot 10^5$	0.392	$4.884 \cdot 10^{-3}$
⋮	⋮	⋮	⋮	⋮	⋮
Case 3	40.12	$0.575 \cdot 10^6$	$1.268 \cdot 10^5$	0.395	$4.323 \cdot 10^{-3}$
⋮	⋮	⋮	⋮	⋮	⋮
Case 14	40.12	$0.557 \cdot 10^6$	$1.379 \cdot 10^5$	0.371	$4.091 \cdot 10^{-3}$
⋮	⋮	⋮	⋮	⋮	⋮
Case 20	40.12	$0.555 \cdot 10^6$	$1.395 \cdot 10^5$	0.385	$4.093 \cdot 10^{-3}$

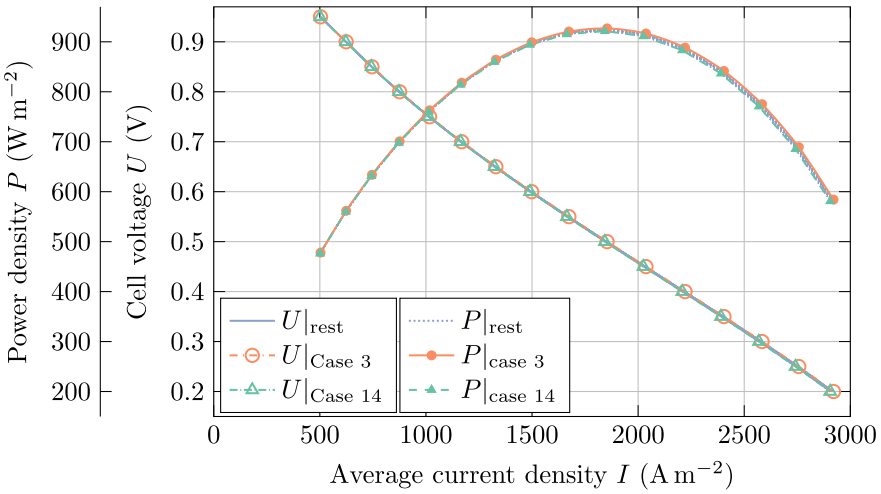

Fig. 8. SOFC performance curves of the optimized point $\mathcal{X}^{\text{opt}}|_{\text{step}=2}$. The effective properties $\mathcal{P}_{\text{eff}}$ of the reconstructions are implemented in the macroscopic model using COMSOL Multiphysics: The polarization curve (U–I) and power density curve (P–I) are evaluated for each reconstruction of the optimized point. Case 3 (orange) with a maximum power of $P^{\text{max}} = 926.85\,\text{W m}^{-2}$ and Case 14 (green) with a maximum power of $P^{\text{max}} = 921.52\,\text{W m}^{-2}$ are shown as best and low performance cases, respectively. The remaining cases "rest" (blue) fall between these two performance curves. (For interpretation of the references to color in this figure legend, the reader is referred to the web version of this article.)

microstructure – identified from only three experimental samples – is determined and characterized. The proposed optimization framework can also be used to optimize a broader range of data sets. For example, it can be used to find the optimal microstructure for a training data set with more diverse electrodes, such as those with different material compositions. To account for mechanical degradation, the mechanical field must be incorporated into microscopic and macroscopic models. In particular, the effective mechanical properties, such as the elasticity tensor, thermal expansion, and creep behavior, must be obtained by homogenization from the microstructure. Additionally, simulating a single solid oxide fuel cell with a mechanical field results in time-dependent stresses in the layers. The surrogate models must be extended to additionally account for the mechanical behavior. The optimization becomes multi-objective since maximizing electric performance and constraining the maximum mechanical stress below a certain stress level are both necessary. To incorporate evolutionary models that capture the microstructure evolution and thus, the electrochemical degradation, the time-dependent behavior would also need to be taken into account within the microscale model.

Besides the integration of experimental data, microstructure characterization and reconstruction, and performance predictions, the sophisticated optimization pipeline offers a high degree of generality. That is, individual methods and modules can be modified or replaced with more suitable techniques for each case study. In the future, several points can be addressed to improve the findings of this work. For instance, (i) more experimental data for different families of microstructures (e.g., different composites) and (ii) uncertainty information in the optimization pipeline can be included. Potential improvements include (iii) the development of nonlinear interpolation methods between the principal components to reconstruct physically plausible and manufacturable microstructure, and (iv) the simultaneous optimization of the anode and the cathode. In addition, (v) the objective function can be extended to include not only electrochemical performance indices, but also mechanical durability key numbers to enhance the mechanical stability of the fuel cell. The ultimate goal, however, is to link the manufacturing process directly to performance metrics. The fabrication process of the layers plays a crucial role for the SOFC performance. To capture the effect of process conditions and powder parameters, such as the particle size and the particle size distribution, (vi) the pipeline of the entire process–structure–property–performance linkages needs to be established in order to optimize process parameters and extend durability beyond 80 000 h.

CRediT authorship contribution statement

Eric Langner: Writing – original draft, Visualization, Validation, Software, Methodology, Investigation, Formal analysis, Conceptualization. **Jakub Lengiewicz:** Writing – original draft, Visualization, Validation, Software, Methodology, Investigation, Formal analysis, Conceptualization. **Artem Semenov:** Writing – review & editing, Methodology, Conceptualization. **Ahmed Makradi:** Methodology, Conceptualization. **Sylvain Gouttebroze:** Methodology, Conceptualization. **Gaston Rauchs:** Methodology, Conceptualization. **Qian Shao:** Methodology, Conceptualization. **Heinz A. Preisig:** Writing – review & editing, Methodology, Conceptualization. **Thomas Wallmersperger:** Writing – review & editing, Resources, Methodology, Funding acquisition, Conceptualization. **Salim Belouettar:** Writing – review & editing, Writing – original draft, Resources, Methodology, Funding acquisition, Conceptualization. **Mohamed El Hachemi:** Writing – original draft, Visualization, Validation, Software, Methodology, Formal analysis, Conceptualization.

Declaration of competing interest

The authors declare that they have no known competing financial interests or personal relationships that could have appeared to influence the work reported in this paper.

Acknowledgments

This work is conducted within the M-ERA.Net project MEDIATE. The MEDIATE project is co-financed by three funding bodies: the Fonds National de la Recherche (FNR, Luxembourg) under grant no. INTER/MER21/16909632/MEDIATE, the Research Council of Norway under grant no. 337560, and the Saxon State Parliament, Germany, with funding provided through tax revenues based on the approved state budget. The authors gratefully acknowledge the support of these funding agencies and the computing time provided by the high-performance computers Barnard at the NHR Centers NHR@TUD. This is funded by the Federal Ministry of Education and Research and the state governments participating on the basis of the resolutions of the GWK for the national high-performance computing at universities (www.nhr-verein.de/unsere-partner). Open access funding enabled and organized by Projekt DEAL.

Data availability

Data will be made available on request.

References

[1] A. Crotwell, L. Gatti, A. Inness, E. Koffi, C. Labuschagne, X. Lan, S. Lee, I. Luijkx, J. Miller, A. Agusti-Panareda, M. Parrington, M. Sasakawa, P. Sperlich, O. Tarasova, K. Tsuboi, A. Vermeulen, A. Visser, F. Vogel, T. Warneke, R. Weiss, C. Yver, X. Lan, H. Chen, A. Vermeulen, K. Tsuboi, O. Tarasova, The State of Greenhouse Gases in the Atmosphere Based on Global Observations through 2024, Greenhouse Gas Bulletin 21, World Meteorological Organization, Geneva, Switzerland, 2025, pp. 1–10, URL https://wmo.int/files/greenhouse-gas-bulletin-no-21.

[2] A. Choudhury, H. Chandra, A. Arora, Application of solid oxide fuel cell technology for power generation—A review, Renew. Sustain. Energy Rev. 20 (2013) 430–442, http://dx.doi.org/10.1016/j.rser.2012.11.031.

[3] M.A. Abdelkareem, K. Elsaid, T. Wilberforce, M. Kamil, E.T. Sayed, A. Olabi, Environmental aspects of fuel cells: A review, Sci. Total Environ. 752 (2021) 141803, http://dx.doi.org/10.1016/j.scitotenv.2020.141803.

[4] P. Pawłowski, S. Buchaniec, T. Prokop, H. Iwai, G. Brus, Microstructure evolution of Solid Oxide Fuel Cell anodes characterized by persistent homology, Energy AI 14 (2023) 100256, http://dx.doi.org/10.1016/j.egyai.2023.100256.

[5] L. Holzer, O. Pecho, T. Hocker, B. Iwanschitz, A. Mai, FIB-tomography data of Ni-YSZ anodes for Solid Oxide Fuel Cells (SOFC): Comparison of pristine and degraded materials (before/after redox cycling), 2020, http://dx.doi.org/10.5281/ZENODO.4056537.

[6] M. Peksen, D. Meric, A. Al-Masri, D. Stolten, A 3D multiphysics model and its experimental validation for predicting the mixing and combustion characteristics of an afterburner, Int. J. Hydrog. Energy 40 (30) (2015) 9462–9472, http://dx.doi.org/10.1016/j.ijhydene.2015.05.103.

[7] A. Semenov, E. Langner, M. El Hachemi, S. Belouettar, T. Wallmersperger, Modelling and simulation of the electro-chemo-thermo-mechanical behaviour of solid oxide fuel cells considering creep, Acta Mech. (2025) 1–19, http://dx.doi.org/10.1007/s00707-025-04334-5.

[8] F. Tariq, E. Ruiz-Trejo, A. Bertei, P. Boldrin, N.P. Brandon, Microstructural Degradation: Mechanisms, Quantification, Modeling and Design Strategies to Enhance the durability of Solid Oxide Fuel Cell Electrodes, in: Solid Oxide Fuel Cell Lifetime and Reliability, Elsevier, 2017, pp. 79–99, http://dx.doi.org/10.1016/B978-0-08-101102-7.00005-2.

[9] S.Z. Golkhatmi, M.I. Asghar, P.D. Lund, A review on solid oxide fuel cell durability: Latest progress, mechanisms, and study tools, Renew. Sustain. Energy Rev. 161 (2022) 112339, http://dx.doi.org/10.1016/j.rser.2022.112339.

[10] M. Saied, K. Ahmed, M. Nemat-Alla, M. Ahmed, M. El-Sebaie, Performance study of solid oxide fuel cell with various flow field designs: numerical study, Int. J. Hydrog. Energy 43 (45) (2018) 20931–20946, http://dx.doi.org/10.1016/j.ijhydene.2018.09.034.

[11] K. Ren, Y. Su, Z. Zhong, Z. Jiao, Microstructure-insight topology optimization for efficient interconnect flow channels in solid oxide fuel cells, Int. J. Heat Mass Transfer 242 (2025) 126823, http://dx.doi.org/10.1016/j.ijheatmasstransfer.2025.126823.

[12] V. Subotić, M. Eibl, C. Hochenauer, Artificial intelligence for time-efficient prediction and optimization of solid oxide fuel cell performances, Energy Convers. Manage. 230 (2021) 113764, http://dx.doi.org/10.1016/j.enconman.2020.113764.

[13] J. Baek, J. Kim, H. Lee, M. Lee, M. Choi, Bayesian-optimization-assisted efficient operation for direct ammonia solid oxide fuel cells, J. Power Sources 619 (2024) 235194, http://dx.doi.org/10.1016/j.jpowsour.2024.235194.

[14] H. Wen, J. Ordonez, J. Vargas, Optimization of single SOFC structural design for maximum power, Appl. Therm. Eng. 50 (1) (2013) 12–25, http://dx.doi.org/10.1016/j.applthermaleng.2012.05.020.

[15] A.M. Nassef, A. Fathy, E.T. Sayed, M.A. Abdelkareem, H. Rezk, W.H. Tanveer, A.G. Olabi, Maximizing SOFC performance through optimal parameters identification by modern optimization algorithms, Renew. Energy 138 (2019) 458–464, http://dx.doi.org/10.1016/j.renene.2019.01.072.

[16] L. Xia, A. Khosravi, M. Han, L. Sun, Artificial intelligence based structural optimization of solid oxide fuel cell with three-dimensional reticulated trapezoidal flow field, Int. J. Hydrog. Energy 48 (72) (2023) 28131–28149, http://dx.doi.org/10.1016/j.ijhydene.2023.03.392.

[17] F. Calise, M.D. d'Accadia, L. Vanoli, M.R. von Spakovsky, Full load synthesis/design optimization of a hybrid SOFC–GT power plant, Energy 32 (4) (2007) 446–458, http://dx.doi.org/10.1016/j.energy.2006.06.016.

[18] Z. Hajabdollahi, P.-F. Fu, Multi-objective based configuration optimization of SOFC-GT cogeneration plant, Appl. Therm. Eng. 112 (2017) 549–559, http://dx.doi.org/10.1016/j.applthermaleng.2016.10.103.

[19] A.V. Virkar, J. Chen, C.W. Tanner, J.-W. Kim, The role of electrode microstructure on activation and concentration polarizations in solid oxide fuel cells, Solid State Ion. 131 (1–2) (2000) 189–198, http://dx.doi.org/10.1016/S0167-2738(00)00633-0.

[20] J.S. Cronin, J.R. Wilson, S.A. Barnett, Impact of pore microstructure evolution on polarization resistance of Ni-Yttria-stabilized zirconia fuel cell anodes, J. Power Sources 196 (5) (2011) 2640–2643, http://dx.doi.org/10.1016/j.jpowsour.2010.10.084.

[21] N. Vivet, S. Chupin, E. Estrade, A. Richard, S. Bonnamy, D. Rochais, E. Bruneton, Effect of Ni content in SOFC Ni-YSZ cermets: A three-dimensional study by FIB-SEM tomography, J. Power Sources 196 (23) (2011) 9989–9997, http://dx.doi.org/10.1016/j.jpowsour.2011.07.010.

[22] O. Pecho, A. Mai, B. Münch, T. Hocker, R. Flatt, L. Holzer, 3D microstructure effects in Ni-YSZ anodes: Influence of TPB lengths on the electrochemical performance, Materials 8 (10) (2015) 7129–7144, http://dx.doi.org/10.3390/ma8105370.

[23] L. Holzer, B. Iwanschitz, T. Hocker, L. Keller, O. Pecho, G. Sartoris, P. Gasser, B. Muench, Redox cycling of Ni–YSZ anodes for solid oxide fuel cells: Influence of tortuosity, constriction and percolation factors on the effective transport properties, J. Power Sources 242 (2013) 179–194, http://dx.doi.org/10.1016/j.jpowsour.2013.05.047.

[24] Y. Ji, K. Yuan, J. Chung, Monte-Carlo simulation and performance optimization for the cathode microstructure in a solid oxide fuel cell, J. Power Sources 165 (2) (2007) 774–785, http://dx.doi.org/10.1016/j.jpowsour.2006.12.058.

[25] A. Faes, J.-M. Fuerbringer, D. Mohamedi, A. Hessler-Wyser, G. Caboche, J. Van Herle, Design of experiment approach applied to reducing and oxidizing tolerance of anode supported solid oxide fuel cell. Part I: Microstructure optimization, J. Power Sources 196 (17) (2011) 7058–7069, http://dx.doi.org/10.1016/j.jpowsour.2010.07.092.

[26] P.A. Connor, X. Yue, C.D. Savaniu, R. Price, G. Triantafyllou, M. Cassidy, G. Kerherve, D.J. Payne, R.C. Maher, L.F. Cohen, R.I. Tomov, B.A. Glowacki, R.V. Kumar, J.T.S. Irvine, Tailoring SOFC electrode microstructures for improved performance, Adv. Energy Mater. 8 (23) (2018) 1800120, http://dx.doi.org/10.1002/aenm.201800120.

[27] C. Bischof, A. Nenning, A. Malleier, L. Martetschläger, A. Gladbach, W. Schafbauer, A.K. Opitz, M. Bram, Microstructure optimization of nickel/gadolinium-doped ceria anodes as key to significantly increasing power density of metal-supported solid oxide fuel cells, Int. J. Hydrog. Energy 44 (59) (2019) 31475–31487, http://dx.doi.org/10.1016/j.ijhydene.2019.10.010.

[28] D. Mohanty, J.-Y. Hung, Y.-W. Chen, I.-M. Hung, Y.-R. Lin, Optimization and characterization of porous Ni/YSZ anode microstructure for solid oxide fuel cell, Ceram. Int. 51 (16, Part B) (2025) 22841–22848, http://dx.doi.org/10.1016/j.ceramint.2025.02.021, 8th International Symposium on Advanced Ceramics and Technology for Sustainable Engineering Applications (ACTSEA-2024).

[29] S. Lee, J. Hwang, W. Yu, S. Ryu, S.W. Cha, Optimizing Ni-YSZ microstructure through anodic aluminum oxide substrate pore size modulation for enhanced reversible solid oxide cell performance, Surf. Coat. Technol. 508 (2025) 132130, http://dx.doi.org/10.1016/j.surfcoat.2025.132130.

[30] E. Langner, H. Dehghani, M. El Hachemi, E. Belouettar-Mathis, A. Makradi, T. Wallmersperger, S. Gouttebroze, H. Preisig, C.W. Andersen, Q. Shao, et al., Physics-based and data-driven modelling and simulation of Solid Oxide Fuel Cells, Int. J. Hydrog. Energy 96 (2024) 962–983, http://dx.doi.org/10.1016/j.ijhydene.2024.10.424.

[31] S. Belouettar, M.E. Hachemi, E. Langner, H. Dahghani, E. Belouettar-Mathis, S. Gouttebroze, A. Makradi, J. Lengiewicz, T. Wallmersperger, H.A. Preisig, et al., 3D and time-dependent simulation of a planar solid oxide fuel cell: bridging microstructure and multiphysics phenomena, Acta Mech. (2025) 1–21, http://dx.doi.org/10.1007/s00707-025-04456-w.
[32] M. Kleitz, F. Petitbon, Optimized SOFC electrode microstructure, Solid State Ion. 92 (1) (1996) 65–74, http://dx.doi.org/10.1016/S0167-2738(96)00464-X.
[33] D.H. Jeon, J.H. Nam, C.-J. Kim, Microstructural optimization of anode-supported Solid Oxide Fuel Cells by a comprehensive microscale model, J. Electrochem. Soc. 153 (2) (2006) A406, http://dx.doi.org/10.1149/1.2139954.
[34] J. Shi, X. Xue, Microstructure optimization designs for anode-supported Planar Solid Oxide Fuel Cells, J. Fuel Cell Sci. Technol. 8 (6) (2011) 061006, http://dx.doi.org/10.1115/1.4004642.
[35] S. Farhad, F. Hamdullahpur, Optimization of the microstructure of porous composite cathodes in solid oxide fuel cells, AIChE J. 58 (4) (2012) 1248–1261, http://dx.doi.org/10.1002/aic.12652.
[36] M.M. Sebdani, M. Baniassadi, J. Jamali, M. Ahadiparast, K. Abrinia, M. Safdari, Designing an optimal 3D microstructure for three-phase solid oxide fuel cell anodes with maximal active triple phase boundary length (TPBL), Int. J. Hydrog. Energy 40 (45) (2015) 15585–15596, http://dx.doi.org/10.1016/j.ijhydene.2015.09.086.
[37] T. Abdullah, L. Liu, Simulation-based microstructural optimization of solid oxide fuel cell for low temperature operation, Int. J. Hydrog. Energy 41 (31) (2016) 13632–13643, http://dx.doi.org/10.1016/j.ijhydene.2016.05.177.
[38] A. Hasanabadi, M. Baniassadi, K. Abrinia, M. Safdari, H. Garmestani, Optimization of solid oxide fuel cell cathodes using two-point correlation functions, Comput. Mater. Sci. 123 (2016) 268–276, http://dx.doi.org/10.1016/j.commatsci.2016.07.004.
[39] S. Buchaniec, A. Sciazko, M. Mozdzierz, G. Brus, A novel approach to the optimization of a solid oxide fuel cell anode using evolutionary algorithms, IEEE Access 7 (2019) 34361–34372, http://dx.doi.org/10.1109/ACCESS.2019.2904327.
[40] Z. Yan, A. He, S. Hara, N. Shikazono, Modeling of solid oxide fuel cell (SOFC) electrodes from fabrication to operation: Microstructure optimization via artificial neural networks and multi-objective genetic algorithms, Energy Convers. Manage. 198 (2019) 111916, http://dx.doi.org/10.1016/j.enconman.2019.111916.
[41] Q. Li, G. Cao, X. Zhang, G. Li, Topology optimization of the microstructure of solid oxide fuel cell cathodes, Acta Mater. 201 (2020) 278–285, http://dx.doi.org/10.1016/j.actamat.2020.10.003.
[42] Z. Yan, A. He, S. Hara, N. Shikazono, Design and optimization of functionally graded electrodes for solid oxide fuel cells (SOFCs) by mesoscale modeling, Int. J. Hydrog. Energy 47 (37) (2022) 16610–16625, http://dx.doi.org/10.1016/j.ijhydene.2022.03.165.
[43] L. Duan, Z. Yan, Z. Pan, Z. Zhong, Microstructure-informed performance boost in solid oxide fuel cells through multiphysical modeling and machine learning, J. Mater. Chem. A 13 (34) (2025) 28471–28482, http://dx.doi.org/10.1039/D5TA03421C.
[44] D. Ruiz-Perez, H. Guan, P. Madhivanan, K. Mathee, G. Narasimhan, So you think you can PLS-DA? BMC Bioinformatics 21 (1) (2020) 2, http://dx.doi.org/10.1186/s12859-019-3310-7.
[45] P. Benner, A. Cohen, M. Ohlberger, K. Willcox, Model Reduction and Approximation: Theory and Algorithms, Society for Industrial and Applied Mathematics, 2017, http://dx.doi.org/10.1137/1.9781611974829.
[46] M. Barker, W. Rayens, Partial least squares for discrimination, J. Chemom. 17 (3) (2003) 166–173, http://dx.doi.org/10.1002/cem.785.
[47] R.G. Brereton, G.R. Lloyd, Partial least squares discriminant analysis: taking the magic away, J. Chemom. 28 (4) (2014) 213–225, http://dx.doi.org/10.1002/cem.2609.
[48] R. Maulik, T. Botsas, N. Ramachandra, L.R. Mason, I. Pan, Latent-space time evolution of non-intrusive reduced-order models using Gaussian process emulation, Phys. D: Nonlinear Phenom. 416 (2021) 132797, http://dx.doi.org/10.1016/j.physd.2020.132797.
[49] J. Donnelly, A. Daneshkhah, S. Abolfathi, Forecasting global climate drivers using Gaussian processes and convolutional autoencoders, Eng. Appl. Artif. Intell. 128 (2024) 107536, http://dx.doi.org/10.1016/j.engappai.2023.107536.
[50] J. Masci, U. Meier, D. Cireşan, J. Schmidhuber, Stacked convolutional auto-encoders for hierarchical feature extraction, in: Artificial Neural Networks and Machine Learning–ICANN 2011: 21st International Conference on Artificial Neural Networks, Espoo, Finland, June 14–17, 2011, Proceedings, Part I 21, Springer, 2011, pp. 52–59, http://dx.doi.org/10.1007/978-3-642-21735-7_7.
[51] C.-Y. Liou, W.-C. Cheng, J.-W. Liou, D.-R. Liou, Autoencoder for words, Neurocomputing 139 (2014) 84–96, http://dx.doi.org/10.1016/j.neucom.2013.09.055.
[52] S. Deshpande, H. Rappel, M. Hobbs, S.P.A. Bordas, J. Lengiewicz, Gaussian process regression + deep neural network autoencoder for probabilistic surrogate modeling in nonlinear mechanics of solids, Comput. Methods Appl. Mech. Engrg. 437 (2025) 117790, http://dx.doi.org/10.1016/j.cma.2025.117790.
[53] R. Storn, K. Price, Differential evolution – A simple and efficient heuristic for global optimization over continuous spaces, J. Global Optim. 11 (4) (1997) 341–359, http://dx.doi.org/10.1023/a:1008202821328.
[54] G. Blatman, B. Sudret, Adaptive sparse polynomial chaos expansion based on least angle regression, J. Comput. Phys. 230 (6) (2011) 2345–2367, http://dx.doi.org/10.1016/j.jcp.2010.12.021.
[55] M.J.D. Powell, The theory of radial basis function approximation in 1990, in: Advances in Numerical Analysis, Oxford University PressOxford, 1992, pp. 105–210, http://dx.doi.org/10.1093/oso/9780198534396.003.0003.
[56] A.I.J. Forrester, A. Sobester, A.J. Keane, Engineering Design via Surrogate Modelling: A Practical Guide, Wiley, Chichester, 2009, http://dx.doi.org/10.1002/9780470770801.
[57] S.L. Brunton, J.N. Kutz, Data-Driven Science and Engineering: Machine Learning, Dynamical Systems, and Control, Cambridge University Press, 2019, http://dx.doi.org/10.1017/9781108380690.
[58] S. Deshpande, S.P.A. Bordas, J. Lengiewicz, MAgNET: A graph U-Net architecture for mesh-based simulations, Eng. Appl. Artif. Intell. 133 (2024) 108055, http://dx.doi.org/10.1016/j.engappai.2024.108055.
[59] S. Deshpande, R.I. Sosa, S.P.A. Bordas, J. Lengiewicz, Convolution, aggregation and attention based deep neural networks for accelerating simulations in mechanics, Front. Mater. 10 (2023) http://dx.doi.org/10.3389/fmats.2023.1128954.
[60] S. Deshpande, J. Lengiewicz, S.P.A. Bordas, Probabilistic deep learning for real-time large deformation simulations, Comput. Methods Appl. Mech. Engrg. 398 (2022) 115307, http://dx.doi.org/10.1016/j.cma.2022.115307.
[61] C.E. Rasmussen, C.K.I. Williams, Gaussian Processes for Machine Learning, vol. 1, MIT press Cambridge, 2006.
[62] M. Kennedy, A. O'Hagan, Bayesian calibration of computer models, J. R. Stat. Soc.: Series B (Statistical Methodology) 63 (3) (2001) 425–464, http://dx.doi.org/10.1111/1467-9868.00294.
[63] M. Bayarri, J.O. Berger, R. Paulo, J. Sacks, J.A. Cafeo, J. Cavendish, C.H. Lin, J. Tu, A framework for validation of computer models, Technometrics 49 (2) (2007) 138–154, http://dx.doi.org/10.1198/004017007000000092.
[64] P. Arendt, D. Apley, W. Chen, Quantification of model uncertainty: calibration, model discrepancy, and identifiability, J. Mech. Des. 134 (10) (2012) 100908, http://dx.doi.org/10.1115/1.4007390.
[65] A. Vadeboncoeur, I. Kazlauskaite, Y. Papandreou, F. Cirak, M. Girolami, O.D. Akyildiz, Random grid neural processes for parametric partial differential equations, in: A. Krause, E. Brunskill, K. Cho, B. Engelhardt, S. Sabato, J. Scarlett (Eds.), Proceedings of the 40th International Conference on Machine Learning, in: Proceedings of Machine Learning Research, vol. 202, PMLR, 2023, pp. 34759–34778, URL https://proceedings.mlr.press/v202/vadeboncoeur23a.html.
[66] P.S. Koutsourelakis, A multi-resolution, non-parametric, Bayesian framework for identification of spatially-varying model parameters, J. Comput. Phys. 228 (17) (2009) 6184–6211, http://dx.doi.org/10.1016/j.jcp.2009.05.016.
[67] C. Ding, H. Rappel, T. Dodwell, Full-field order-reduced Gaussian Process emulators for nonlinear probabilistic mechanics, Comput. Methods Appl. Mech. Engrg. 405 (2023) 115855, http://dx.doi.org/10.1016/j.cma.2022.115855.
[68] M.L. Stein, Interpolation of Spatial Data: Some Theory for Kriging, Springer, New York, 1999, http://dx.doi.org/10.1007/978-1-4612-1494-6.
[69] E. Langner, P. Seibert, A. Semenov, M. Kästner, T. Wallmersperger, Structure–property relationships of solid oxide fuel cell electrodes using real and reconstructed microstructures, Internat. J. Numer. Methods Engrg. 126 (24) (2025) e70205, http://dx.doi.org/10.1002/nme.70205.
[70] E. Langner, A. Semenov, A. Makradi, S. Gouttebroze, S. Belouettar, T. Wallmersperger, Macroscopic properties of solid oxide fuel cell electrodes via microstructure-based numerical homogenization, PAMM (2024) e202400023, http://dx.doi.org/10.1002/pamm.202400023.
[71] I.A. Baratta, J.P. Dean, J.S. Dokken, M. Habera, J.S. Hale, C.N. Richardson, M.E. Rognes, M.W. Scroggs, N. Sime, G.N. Wells, DOLFINx: the next generation FEniCS problem solving environment, 2023, http://dx.doi.org/10.5281/zenodo.10447666.
[72] R. Mahbub, W.K. Epting, T. Hsu, J.H. Mason, M. Feng, N.T. Nuhfer, H.W. Abernathy, G.A. Hackett, S. Litster, A.D. Rollett, et al., Quantitative analysis of multi-scale heterogeneities in complex electrode microstructures, J. Electrochem. Soc. 167 (5) (2020) 054506, http://dx.doi.org/10.1149/2.0102005JES.
[73] X. Zhang, L. Wang, M. Espinoza, T. Li, M. Andersson, Numerical simulation of solid oxide fuel cells comparing different electrochemical kinetics, Int. J. Energy Res. 45 (9) (2021) 12980–12995, http://dx.doi.org/10.1002/er.6628.
[74] D. Osinkin, D. Bronin, S. Beresnev, N. Bogdanovich, V. Zhuravlev, G. Vdovin, T. Demyanenko, Thermal expansion, gas permeability, and conductivity of Ni-YSZ anodes produced by different techniques, J. Solid State Electrochem. 18 (1) (2014) 149–156, http://dx.doi.org/10.1007/s10008-013-2239-4.
[75] T. Yonekura, Y. Tachikawa, T. Yoshizumi, Y. Shiratori, K. Ito, K. Sasaki, Exchange current density of solid oxide fuel cell electrodes, ECS Trans. 35 (1) (2011) 1007, http://dx.doi.org/10.1149/1.3570081.
[76] A. Perna, M. Minutillo, E. Jannelli, V. Cigolotti, S.W. Nam, K.J. Yoon, Performance assessment of a hybrid SOFC/MGT cogeneration power plant fed by syngas from a biomass down-draft gasifier, Appl. Energy 227 (2018) 80–91, http://dx.doi.org/10.1016/j.apenergy.2017.08.077.
[77] R. Fernández-González, E. Hernández, S. Savvin, P. Núñez, A. Makradi, N. Sabaté, J. Esquivel, J. Ruiz-Morales, A novel microstructured metal-supported solid oxide fuel cell, J. Power Sources 272 (2014) 233–238, http://dx.doi.org/10.1016/j.jpowsour.2014.08.081.

[78] Q. Shao, R. Fernández-González, J. Ruiz-Morales, L. Bouhala, D. Fiorelli, A. Younes, P. Núñez, S. Belouettar, A. Makradi, An advanced numerical model for energy conversion and crack growth predictions in Solid Oxide Fuel Cell units, Int. J. Hydrog. Energy 40 (46) (2015) 16509–16520, http://dx.doi.org/10.1016/j.ijhydene.2015.10.016.

[79] P. Seibert, A. Raßloff, K. Kalina, M. Ambati, M. Kästner, Microstructure characterization and reconstruction in Python: MCRpy, Integr. Mater. Manuf. Innov. 11 (3) (2022) 450–466, http://dx.doi.org/10.1007/s40192-022-00273-4.

[80] K. Machaj, J. Kupecki, A. Niemczyk, Z. Malecha, J. Brouwer, D. Porwisiak, Numerical analysis of the relation between the porosity of the fuel electrode support and functional layer, and performance of solid oxide fuel cells using computational fluid dynamics, Int. J. Hydrog. Energy 52 (2024) 936–951, http://dx.doi.org/10.1016/j.ijhydene.2023.06.166.

[81] S.P. Jiang, Development of lanthanum strontium cobalt ferrite perovskite electrodes of solid oxide fuel cells–A review, Int. J. Hydrog. Energy 44 (14) (2019) 7448–7493, http://dx.doi.org/10.1016/j.ijhydene.2019.01.212.

[82] M. Iwata, T. Hikosaka, M. Morita, T. Iwanari, K. Ito, K. Onda, Y. Esaki, Y. Sakaki, S. Nagata, Performance analysis of planar-type unit SOFC considering current and temperature distributions, Solid State Ion. 132 (3–4) (2000) 297–308, http://dx.doi.org/10.1016/S0167-2738(00)00645-7.

[83] W. Kong, Q. Zhang, X. Xu, D. Chen, A simple expression for the tortuosity of gas transport paths in solid oxide fuel cells' porous electrodes, Energies 8 (12) (2015) 13953–13959, http://dx.doi.org/10.3390/en81212406.

[84] P. Costamagna, P. Costa, V. Antonucci, Micro-modelling of solid oxide fuel cell electrodes, Electrochim. Acta 43 (3–4) (1998) 375–394, http://dx.doi.org/10.1016/S0013-4686(97)00063-7.

[85] S.B. Beale, M. Andersson, C. Boigues-Muñoz, H.L. Frandsen, Z. Lin, S.J. McPhail, M. Ni, B. Sundén, A. Weber, A.Z. Weber, Continuum scale modelling and complementary experimentation of solid oxide cells, Prog. Energy Combust. Sci. 85 (2021) 100902, http://dx.doi.org/10.1016/j.pecs.2020.100902.

[86] H. Moussaoui, R. Sharma, J. Debayle, Y. Gavet, G. Delette, J. Laurencin, Microstructural correlations for specific surface area and triple phase boundary length for composite electrodes of solid oxide cells, J. Power Sources 412 (2019) 736–748, http://dx.doi.org/10.1016/j.jpowsour.2018.11.095.

[87] D. Simwonis, H. Thülen, F. Dias, A. Naoumidis, D. Stöver, Properties of Ni/YSZ porous cermets for SOFC anode substrates prepared by tape casting and coatmix® process, J. Mater. Process. Technol. 92 (1999) 107–111, http://dx.doi.org/10.1016/S0924-0136(99)00214-9.